JGR Planets

RESEARCH ARTICLE
10.1029/2021JE007096

Special Section:
The Curiosity rover's investigation of Glen Torridon and the surrounding area

Orbital and In-Situ Investigation of Periodic Bedrock Ridges in Glen Torridon, Gale Crater, Mars

Kathryn M. Stack[1], William E. Dietrich[2], Michael P. Lamb[3], Robert J. Sullivan[4], John R. Christian[5], Claire E. Newman[6], Catherine D. O'Connell-Cooper[7], Jonathan W. Sneed[8], Mackenzie Day[8], Mariah Baker[9], Raymond E. Arvidson[5], Christopher M. Fedo[10], Sabrina Khan[11], Rebecca M. E. Williams[12], Kristen A. Bennett[13], Alexander B. Bryk[2], Shannon Cofield[14], Lauren A. Edgar[13], Valerie K. Fox[15], Abigail A. Fraeman[1], Christopher H. House[16], David M. Rubin[17], Vivian Z. Sun[1], and Jason K. Van Beek[1]

[1]Jet Propulsion Laboratory, California Institute of Technology, Pasadena, CA, USA, [2]Department of Earth and Planetary Science, University of California, Berkeley, Berkeley, CA, USA, [3]Division of Geological and Planetary Sciences, California Institute of Technology, Pasadena, CA, USA, [4]Cornell Center for Astrophysics & Planetary Science, Cornell University, Ithaca, NY, USA, [5]Department of Earth and Planetary Sciences, Washington University in St. Louis, St. Louis, MO, USA, [6]Aeolis Research, Chandler, AZ, USA, [7]Department of Earth Science, University of New Brunswick, Fredericton, NB, Canada, [8]Department of Earth, Planetary, and Space Sciences, University of California, Los Angeles, Los Angeles, CA, USA, [9]Center for Earth & Planetary Studies, National Air & Space Museum, Smithsonian Institution, Washington, DC, USA, [10]Department of Earth and Planetary Sciences, University of Tennessee, Knoxville, Knoxville, TN, USA, [11]Department of Earth, Atmospheric, and Planetary Sciences, Massachusetts Institute of Technology, Cambridge, MA, USA, [12]Planetary Science Institute, Tucson, AZ, USA, [13]Astrogeology Science Center, U.S. Geological Survey, Flagstaff, AZ, USA, [14]U.S. Department of the Interior, Bureau of Ocean Energy Management, Washington, DC, USA, [15]Earth and Environmental Sciences, University of Minnesota, Minneapolis, MN, USA, [16]College of Earth and Mineral Sciences, Penn State University, University Park, PA, USA, [17]Earth and Planetary Sciences, University of California, Santa Cruz, Santa Cruz, CA, USA

Key Points:

- Decameter-long, regularly spaced bedrock ridges oriented northeast-southwest occur throughout the Glen Torridon region of Aeolis Mons
- Glen Torridon ridges cross-cut elevation contours and bedding, exhibit bifurcations, and are disrupted by small impact craters
- Glen Torridon ridges are erosional periodic bedrock ridges whose formation places erosional and depositional constraints on Aeolis Mons

Correspondence to:
K. M. Stack,
kathryn.m.stack@jpl.nasa.gov

Citation:
Stack, K. M., Dietrich, W. E., Lamb, M. P., Sullivan, R. J., Christian, J. R., Newman, C. E., et al. (2022). Orbital and in-situ investigation of periodic bedrock ridges in Glen Torridon, Gale Crater, Mars. *Journal of Geophysical Research: Planets*, *127*, e2021JE007096. https://doi.org/10.1029/2021JE007096

Received 18 OCT 2021
Accepted 7 MAY 2022

Author Contributions:
Conceptualization: William E. Dietrich, Michael P. Lamb, Robert J. Sullivan, Mackenzie Day, Christopher M. Fedo, Rebecca M. E. Williams
Formal analysis: Robert J. Sullivan, John R. Christian, Claire E. Newman
Investigation: William E. Dietrich, Michael P. Lamb, Robert J. Sullivan, John R. Christian, Catherine D.

Abstract Gale crater, the field site for NASA's Mars Science Laboratory Curiosity rover, contains a diverse and extensive record of aeolian deposition and erosion. This study focuses on a series of regularly spaced, curvilinear, and sometimes branching bedrock ridges that occur within the Glen Torridon region on the lower northwest flank of Aeolis Mons, the central mound within Gale crater. During Curiosity's exploration of Glen Torridon between sols ~2300–3080, the rover drove through this field of ridges, providing the opportunity for in situ observation of these features. This study uses orbiter and rover data to characterize ridge morphology, spatial distribution, compositional and material properties, and association with other aeolian features in the area. Based on these observations, we find that the Glen Torridon ridges are consistent with an origin as wind-eroded bedrock ridges, carved during the exhumation of Mount Sharp. Erosional features like the Glen Torridon ridges observed elsewhere on Mars, termed periodic bedrock ridges (PBRs), have been interpreted to form transverse to the dominant wind direction. The size and morphology of the Glen Torridon PBRs are consistent with transverse formative winds, but the orientation of nearby aeolian bedforms and bedrock erosional features raise the possibility of PBR formation by a net northeasterly wind regime. Although several formation models for the Glen Torridon PBRs are still under consideration, and questions persist about the nature of PBR-forming paleowinds, the presence of PBRs at this site provides important constraints on the depositional and erosional history of Gale crater.

Plain Language Summary Wind has played a major role in sculpting the surface of Mars. Gale crater, the field site for NASA's Mars Science Laboratory Curiosity rover since it landed there in 2012, contains a vast and varied record of deposition and erosion by the wind. This study focuses on a series of regularly spaced, generally straight bedrock ridges that occur within the clay-bearing Glen Torridon region of Aeolis Mons (informally named Mount Sharp) in Gale crater. During Curiosity's exploration of the Glen Torridon region between sols ~2300–3080 of the mission, the rover drove through this field of ridges, acquiring images and compositional observations along the way. This study characterizes the Glen Torridon ridges using orbiter and rover data to determine their shape, size, occurrence, and relationship to other wind-formed features in the area. We find that the Glen Torridon ridges were carved by wind into the bedrock of Mount Sharp. Questions remain about the winds that formed these ridges, but this study provides important

O'Connell-Cooper, Jonathan W. Sneed, Mariah Baker, Raymond E. Arvidson, Christopher M. Fedo, Sabrina Khan, Rebecca M. E. Williams, Kristen A. Bennett, Alexander B. Bryk, Shannon Cofield, Lauren A. Edgar, Valerie K. Fox, Abigail A. Fraeman, Christopher H. House, David M. Rubin, Vivian Z. Sun, Jason K. Van Beek
Methodology: William E. Dietrich, Robert J. Sullivan, John R. Christian, Claire E. Newman, Jonathan W. Sneed, Mariah Baker, Sabrina Khan
Writing – original draft: John R. Christian, Claire E. Newman
Writing – review & editing: William E. Dietrich, Michael P. Lamb, Robert J. Sullivan, Catherine D. O'Connell-Cooper, Mackenzie Day, Mariah Baker, Christopher M. Fedo, Rebecca M. E. Williams, Kristen A. Bennett, Alexander B. Bryk, Lauren A. Edgar, Abigail A. Fraeman

information about the history and environment of Gale crater and reports the first rover observations of this type of erosional feature on Mars.

1. Introduction

Wind has been a significant agent of landscape modification during the past several billion years on Mars. A diversity of aeolian landforms are observable on the surface of Mars today, ranging from modern to ancient, familiar to unusual, and micro- to megascale. Such features, which include wind streaks (Arvidson, 1974; Thomas et al., 1981; Veverka et al., 1981), ripples (Bridges et al., 2007; Greeley et al., 1992, 1999; Sullivan et al., 2005, 2008), dunes (Bridges & Ehlmann, 2018; Cutts & Smith, 1973; Hayward et al., 2007; Ward et al., 1985), transverse aeolian ridges (TARs; Balme et al., 2008; Berman et al., 2011, 2018; Geissler, 2014; Geissler & Wilgus, 2017; Zimbelman, 2010), a variety of ventifacts (e.g., Bridges et al., 2014), yardangs (Bridges et al., 2007; Malin et al., 1998; McCauley, 1973; Ward, 1979; Zimbelman & Griffin, 2010), periodic bedrock ridges (PBRs; Favaro et al., 2021; Hugenholtz et al., 2015; Montgomery et al., 2012; Silvestro et al., 2021), aeolian cross-stratification (Anderson et al., 2018; Banham et al., 2018; Ewing et al., 2010; Milliken et al., 2010), and paleobedforms (Chojnacki et al., 2020; Edgett & Malin, 2000; Hunt et al., 2022; Kerber & Head, 2012; Williams & Weitz, 2014) can provide insights into past and present environmental conditions, climate evolution, and depositional and erosional processes on Mars.

Gale crater, the field site for NASA's Mars Science Laboratory (MSL) Curiosity rover since it landed there in 2012, contains an extensive record of aeolian deposition and landscape modification by wind. At the largest scale is the central mountain of Gale crater, Aeolis Mons (informally named "Mount Sharp"), that likely owes much of its current surface relief to excavation by aeolian abrasion and deflation (Grotzinger et al., 2015; Kite et al., 2013; Malin & Edgett, 2000), as well as the crater's wind streak which extends hundreds of kilometers to the south (Day & Kocurek, 2016). Gale crater also contains extensive km-scale dune fields and sandsheets located throughout the crater (Day & Kocurek, 2016; Hobbs et al., 2010; Thomson et al., 2011; Tirsch et al., 2011), including the Bagnold dune field explored on the ground by Curiosity (Bridges & Ehlmann, 2018; Lapotre & Rampe, 2018) and the Sands of Forvie sand sheet (Sullivan, Baker, et al., 2020; Weitz et al., 2021). Ripples at a variety of scales have been observed in orbiter images and on the ground by Curiosity (e.g., Day & Kocurek, 2016; Lapotre et al., 2016; Weitz et al., 2018). Large, bright bedforms identified as TARs by Day and Kocurek (2016) have been observed throughout Gale crater, and similar features have been interpreted as coarse-grained megaripples where observed on the ground by Curiosity (Sullivan, Baker, et al., 2020; Weitz et al., 2018, 2021; Zimbelman & Foroutan, 2020). Large, indurated aeolian features within Gale crater include yardangs—streamlined ridges formed by unidirectional, persistent, flow-parallel wind abrasion—which are concentrated almost exclusively on the flanks of Mount Sharp (Anderson & Bell, 2010; Day & Kocurek, 2016; Dromart et al., 2021), as well as indurated ridges interpreted as preserved paleobedforms (Milliken et al., 2014). The rock record preserved within the central mound of Gale crater also records evidence of ancient aeolian deposition observed both from orbit (Anderson & Bell, 2010; Anderson et al., 2018; Dromart et al., 2021; Le Deit et al., 2013; Milliken et al., 2014; Thomson et al., 2011) and on the ground (Banham, Gupta, Bryk, et al., 2021; Banham, Gupta, Rubin, et al., 2021; Banham et al., 2018; Edgar et al., 2017). Millimeter- to cm-scale evidence of aeolian modification is observed in Gale crater in the form of ventifacts including lineations, facets, and elongated flutes and pits (Bridges et al., 2013; Day & Kocurek, 2016; Sullivan, Baker, et al., 2020). The most recent indicators of aeolian activity in Gale crater are observed in movement of sand within Curiosity's workspaces (Baker, Lapotre, Minitti, et al., 2018; Sullivan, Baker, et al., 2020; Schieber et al., 2020).

This study focuses on a series of regularly spaced, curvilinear, and locally branching ridges that occur within the Fe-smectite clay-bearing "Glen Torridon" region of Mount Sharp (Figure 1). These ridges were first recognized and described in early orbiter-based studies of Gale crater with proposed origins including ancient indurated linear aeolian dunes (Anderson & Bell, 2010; Milliken et al., 2014) or purely erosional features (Anderson & Bell, 2010) with no depositional connection to the Mount Sharp strata in which they occur. Day and Kocurek (2016), the most comprehensive survey to-date of aeolian features within Gale crater, did not include these ridges in their inventory. However, understanding the origin of these ridges—and determining whether they are ancient indurated aeolian dunes or erosional features formed primarily by aeolian processes—can help define primary depositional constraints for this interval of the Mount Sharp stratigraphy, and can provide insight

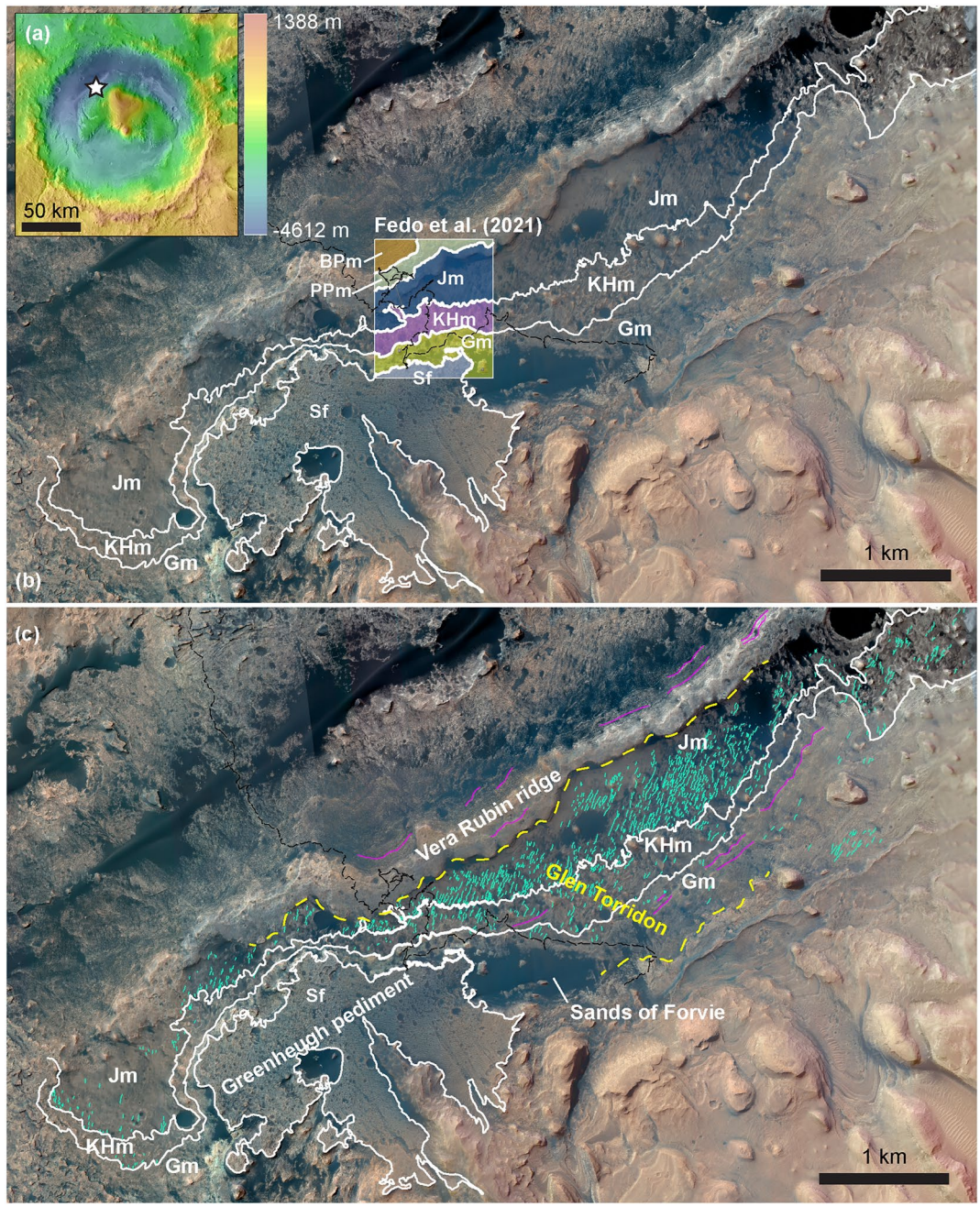

Figure 1. (a) Regional context of the Glen Torridon area within Gale crater shown on a Mars Orbiter Laser Altimeter basemap overlain on THEMIS day IR. (b) Blunts Point (BPm), Pettegrove Point (PPm), and Jura (Jm) members of the Murray formation, Knockfarril Hill (KHm) and Glasgow (Gm) members of the Carolyn Shoemaker formation, and the Stimson formation (Sf) (Figure 2) mapped with high confidence in the rectangular box by Fedo et al. (2021) on a High Resolution Imaging Science Experiment (HiRISE) color basemap. This study's extrapolations of the Jura, Knockfarril Hill, Glasgow, and Stimson contacts are mapped in white beyond the Fedo et al. (2021) map. (c) Periodic, curvilinear ridges traced (in green) within the Glen Torridon region (outlined and labeled in yellow dashed lines) relative to stratigraphic member contacts mapped in white. Strata traceable in HiRISE images above and below Glen Torridon are annotated in pink. The rover's traverse up to sol 3143 is shown in black. The center coordinate (lat and lon) of the area shown is −4.7289, 137.3964. North is up for panels (a and b).

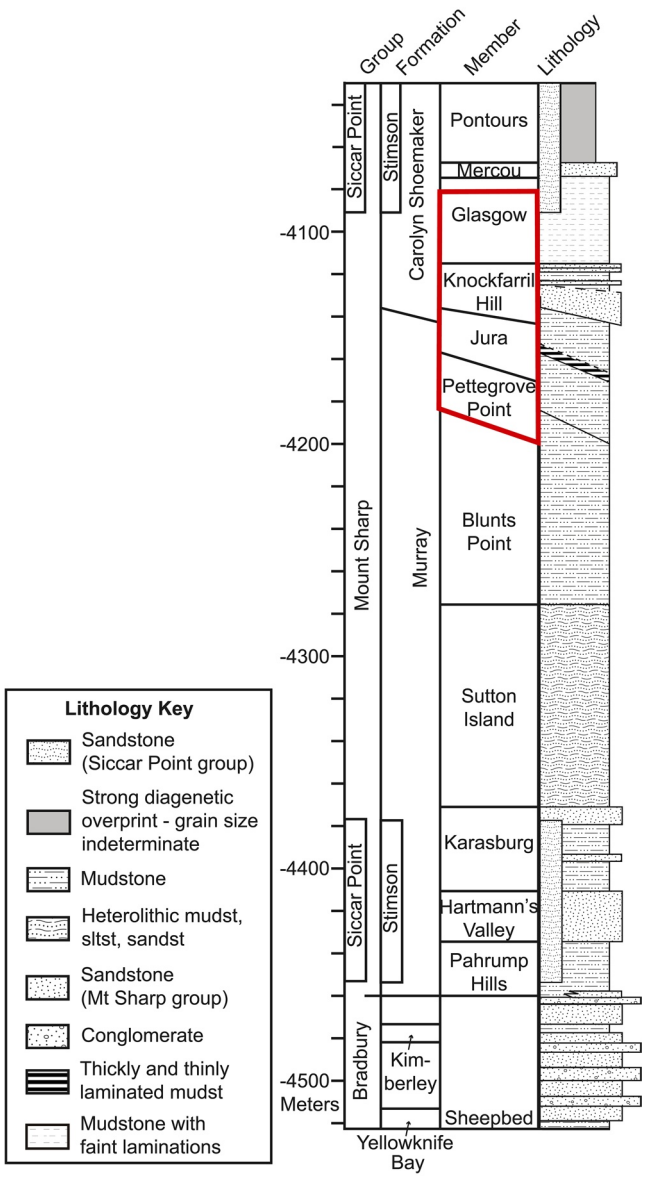

Figure 2. Stratigraphic column modified from Fedo et al. (2019) showing the context of the members cropping out in Vera Rubin ridge and the Glen Torridon area relative to other rocks explored by Curiosity. The members in which the Glen Torridon ridges occur are outlined in red.

into the evolution of environmental conditions within this area of Gale crater. We characterized the Glen Torridon ridges using orbiter data to determine their morphology, spatial distribution, and association with other aeolian features in the area. Morphologic characteristics, composition, and material properties of the ridges were extracted from Curiosity rover data, providing a ground-based perspective on these features. We explored several possible origins for the Glen Torridon ridges and considered the implications of these interpretations for the past depositional context and environmental conditions within Gale crater.

2. Geologic Setting and Mission Context

Since landing on Mars in 2012, the MSL Curiosity rover has explored rock exposures of the floor and central mound of Gale crater, a ~154 km diameter crater located at 5.4°S and 137.8°E along the boundary between Mars' ancient, heavily cratered, southern highlands and its younger, northern lowlands. Curiosity's prime mission was spent exploring mudstones, sandstones, and conglomerates of the "Bradbury" group, representing braided fluvial, deltaic, lacustrine, and aeolian depositional environments (Edgar et al., 2017; Grotzinger et al., 2014; Vasavada et al., 2014; Stack et al., 2016; Rice et al., 2017; Figure 2). Upon reaching the base of Mount Sharp, Curiosity began its exploration of the "Murray" formation, the lowermost unit of the Mount Sharp group (Fedo et al., 2019; Grotzinger et al., 2015; Gwizd et al., 2019; Rivera-Hernández et al., 2019; Stack et al., 2019). During its ascent of lower Mount Sharp, Curiosity also encountered exposures of the "Stimson" formation, an aeolian sandstone of the "Siccar Point" group, deposited unconformably on Mount Sharp strata after the formation of the Gale mound (Banham, Gupta, Bryk, et al., 2021; Banham, Gupta, Rubin, et al., 2021; Banham et al., 2018; Fraeman et al., 2016; Grotzinger et al., 2015).

The Murray formation and overlying "Carolyn Shoemaker" formation have been split into different members defined by variations in lithology, facies, and diagenetic textures (Carvaaca et al., 2021; Fedo et al., 2019; Figure 2). Curiosity's major exploration targets within the Murray formation included the strata of "Vera Rubin" ridge (VRR), an indurated, erosion-resistant ridge exhibiting distinct spectral absorptions attributed to crystalline hematite observed in orbital spectroscopic data (Fraeman et al., 2013), and an E-W elongated trough immediately to the south of VRR called Glen Torridon, in which Fe-smectite clay-bearing Murray bedrock crops out (Bennett et al., 2019; Fox et al., 2021). Strata exposed to the south and up-section of the Glen Torridon area record a transition to sulfate-bearing bedrock observed from orbit (Fraeman et al., 2016; Milliken et al., 2010; Rapin et al., 2021). This transition is hypothesized to record a major, possibly globally significant, shift in the climate of ancient Mars (Bibring et al., 2006; Milliken et al., 2010).

In-situ exploration of VRR by Curiosity between sols 1726 and 2302 revealed that the strata comprising this ridge, designated the "Pettegrove Point" and "Jura" members of the Murray formation, are composed primarily of finely laminated lacustrine mudstones (Edgar et al., 2020). Although the strata that comprise VRR are better indurated than adjacent rocks as a result of diagenesis, they do not exhibit the apparent increase in hematite abundance that was detected by Compact Reconnaissance Imaging Spectrometer for Mars (CRISM) orbital data (Fraeman et al., 2020; Rampe et al., 2020). The Jura member, which consists of the uppermost resistant-to-erosion strata of VRR, extends into more erodible rocks of the Glen Torridon region directly to the south (Bristow et al., 2021; Stein et al., 2020). As Curiosity continued its exploration south, it descended VRR into the Glen

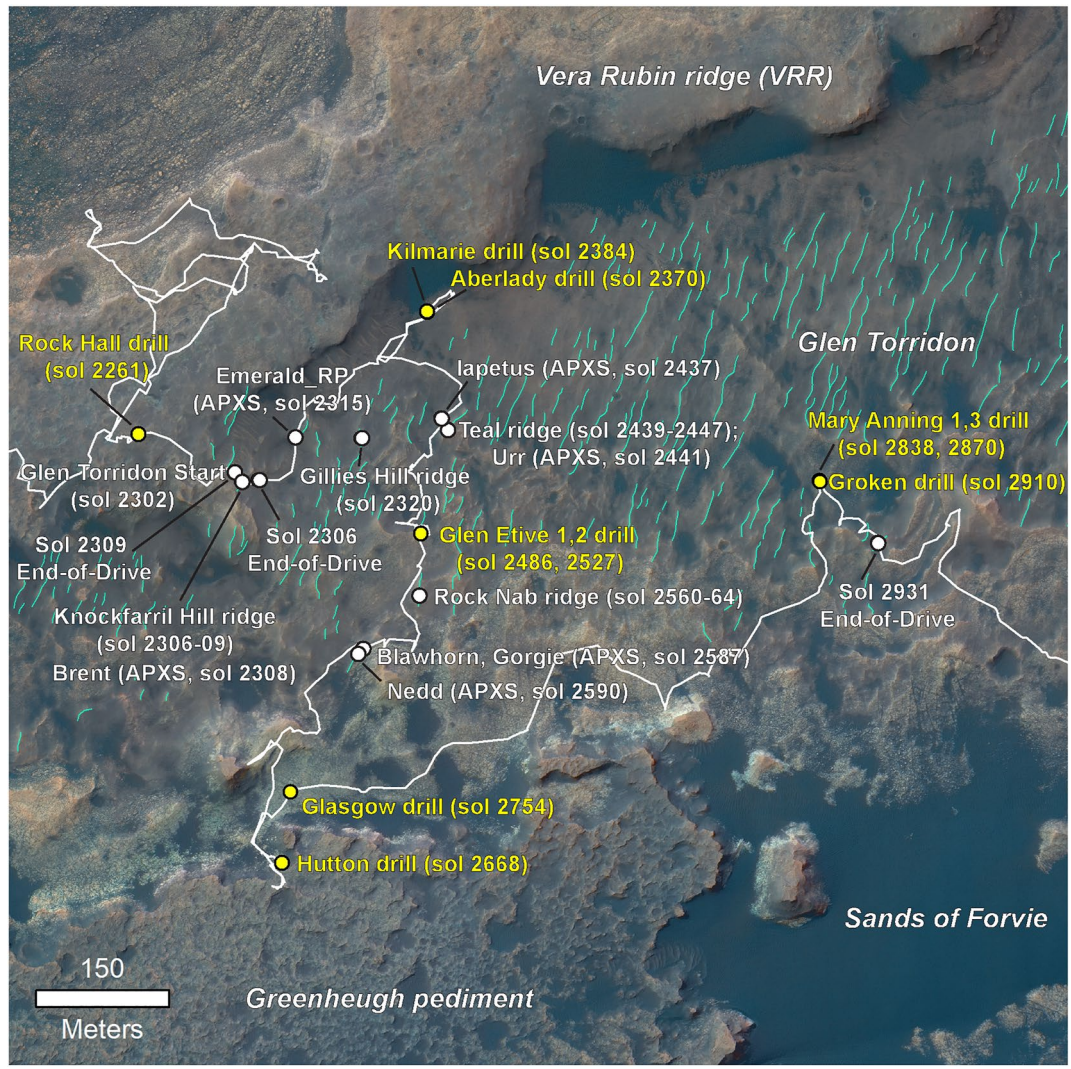

Figure 3. Curiosity's traverse through the Glen Torridon region (white) with the main features and targets (white), and drill locations (yellow) discussed in the paper annotated on a High Resolution Imaging Science Experiment (HiRISE) color basemap. Nearby ridges are traced in green. The center coordinate (lat, lon) of the area shown is −4.7297, 137.3857. HiRISE image IDs: ESP_042682_1755, ESP_039280_1755. North is up.

Torridon area (Figure 3). The rover's exploration of Glen Torridon began on sol 2302, and concluded around sol 3080 (Fox et al., 2021). In-situ exploration by the Curiosity rover revealed that the northern Glen Torridon area is comprised of finely laminated mudstones of the Jura member (Carvaaca et al., 2021), and covered throughout by a regolith layer composed of locally eroding pebble- to cobble-sized clasts (Christian et al., 2022; Khan et al., 2021). There is some uncertainty about the extension of the Pettegrove Point-Jura contact east of the rover's traverse, so it is possible that Pettegrove Point may also be exposed within parts of Glen Torridon. Since the Jura member crops out in both VRR and Glen Torridon, herein it is referred to as either the GT Jura or VRR Jura. Erosion-resistant, cross-bedded sandstones of the "Knockfarril Hill" member of the Carolyn Shoemaker formation overlie the Jura member throughout Glen Torridon, locally eroding into isolated mesas throughout Glen Torridon that transition into more continuous exposures to the south and up stratigraphic section (Carvaaca et al., 2021; Fedo et al., 2019). The Knockfarril Hill member is overlain by the "Glasgow" member of the Carolyn Shoemaker formation (Carvaaca et al., 2021; Fedo et al., 2021) (Figure 2).

In addition to a strong Fe-smectite absorption in orbital spectroscopic data, a distinguishing characteristic of the Glen Torridon region is the presence of regularly spaced, consistently oriented, decameters-long ridges distrib-

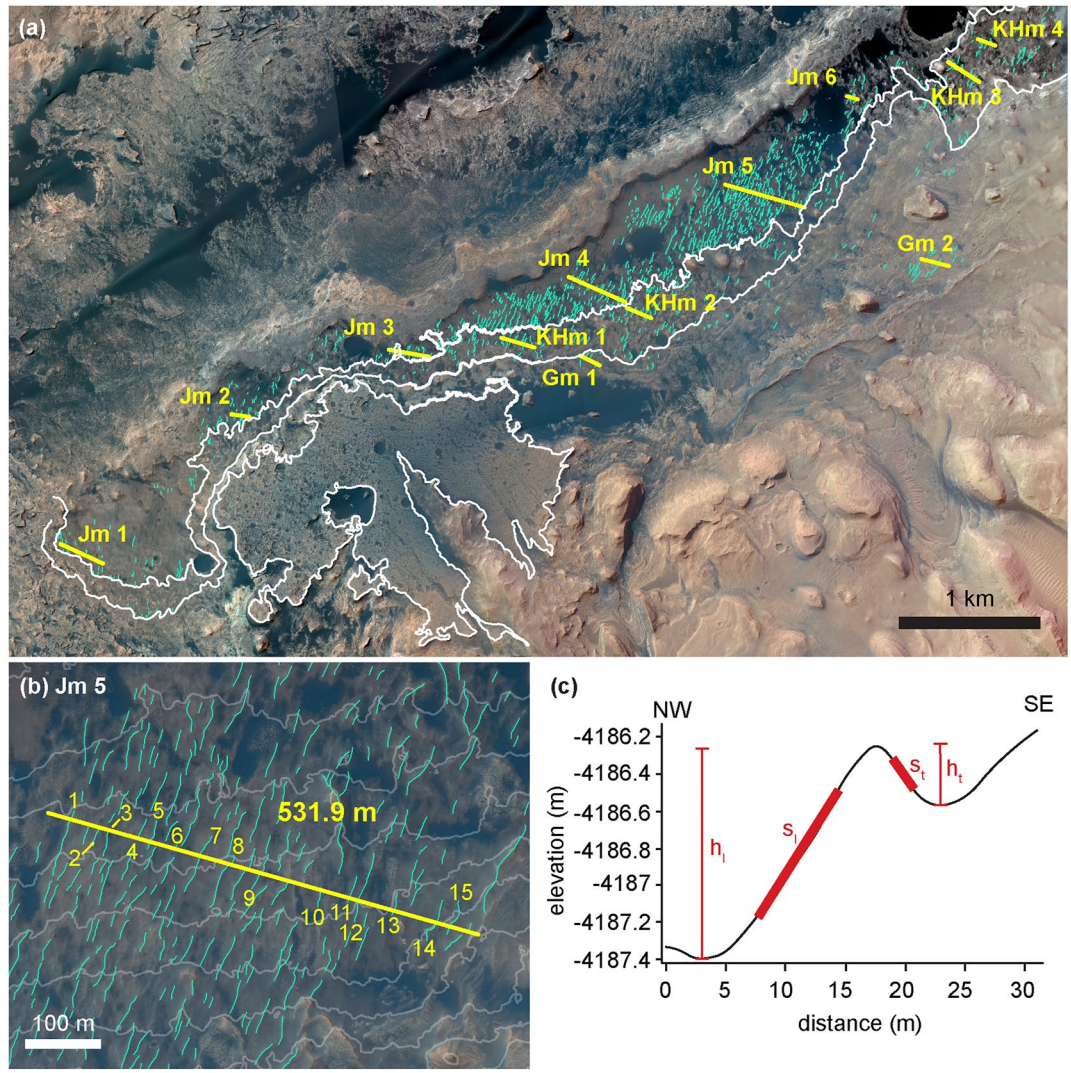

Figure 4. (a) Location of the transects (yellow lines, labeled by member) through Glen Torridon used to calculate ridge spacing reported in Table 1. Jm = Jura member, KHm = Knockfarril Hill member, Gm = Glasgow member. White lines mark the member boundaries in Glen Torridon and the Stimson formation exposed on the Greenheugh pediment. The center coordinate (lat, lon) of the area shown is −4.7289, 137.3964. (b) An example transect with the ridges that cross the transect numbered from 1 to 15. The center coordinate (lat, lon) of the area shown is −4.7125, 137.4184. High Resolution Imaging Science Experiment image ID: ESP_037117_1755. North is up for panels (a and b). (c) A topographic profile extracted from the first ridge of the Jm 5 transect illustrating how height and leading and trailing slope were measured. h_l = leading height, measured as the difference in elevation between the local minimum on the northwest-facing slope and the crest; s_l = slope calculated from the middle half of the leading (typically northwest-facing) slope; s_t = slope calculated from the middle half of the trailing (typically southeast-facing) slope; h_t = trailing height, measured as the difference in elevation between the crest and the local minimum on the southeast-facing slope.

uted across a 2.6 km^2 area spanning nearly eight km laterally (Figure 4). These ridges were first described by Anderson and Bell (2010) who noted similarities between the morphology of the Glen Torridon ridges and aeolian dunes. Anderson and Bell (2010) inferred that the ridges were lithified based on light-toned fractured bedrock comprising some of the ridges, and the presence of occasional impact craters. Anderson and Bell (2010) proposed two possible origins: lithified aeolian bedforms, or soft sedimentary rock eroding in an undulating pattern. The interpretation of these ridges as lithified aeolian bedforms was also supported by Milliken et al. (2014), who interpreted the ridges as indurated remnants of eroded linear bedforms that had been reworked during flooding and burial. Milliken et al.'s (2010) interpretation implied that this interval of the Mount Sharp stratigraphy was aeolian in origin.

3. Data and Methods

The Glen Torridon ridges were mapped and characterized using 25 cm/pixel Mars Reconnaissance Orbiter (MRO; Zurek & Smrekar, 2007) High Resolution Imaging Science Experiment (HiRISE; McEwen et al., 2007) stereo images processed to provide gray-scale (Calef & Parker, 2016b), color, and topographic products (Calef & Parker, 2016a) that were georeferenced and projected according to the methods of Kirk et al. (2008) and Calef et al. (2013). The digital elevation models (DEMs) used in this study have horizontal precisions of 1 m/post, vertical expected precisions (EP) between ∼0.06–0.14 m, and absolute elevations tied to Mars Orbiter Laser Altimeter data. In HiRISE images, 1255 ridges were identified by their relatively straight ridge crests, which typically appear brighter on their sun-facing sides, and their distinct tone compared to dark active aeolian sand fields (Figure 4). Ridge orientation was measured in ESRI's ArcGIS software using the start and end point of each individual ridge. Assuming a positional uncertainty of ∼2 HiRISE pixels (±0.5 m) on the start and end points of a ridge, we estimated an uncertainty in the orientation measurements of no more than a few degrees for an average 30 m long ridge. The uncertainty in orientation measurement increases for shorter ridges (approximately ±20° for the shortest, 3 m-long ridge) and decreases for longer ridges (less than ±0.5° for the longest, ∼200 m ridges).

Ridge spacing was extracted from 12 transects across the Glen Torridon region within the Jura, Knockfarril Hill, and Glasgow members (Figure 4a). Six transects, each spaced ∼1 km apart from east to west, were measured within the Glen Torridon Jura member, 4 transects were measured in the Knockfarril Hill member, and 2 for the Glasgow member (Figure 4a). Because ridges are less common in the Knockfarril Hill and Glasgow members, transects were measured where ridge density was high and relatively uniform to measure several ridges in series. The length of the transect was divided by the number of ridges crossing that transect to calculate mean ridge spacing (Figure 4b, Table 1). We assumed an uncertainty on the length and wavelength measurements of ±1 m, equivalent to 4 HiRISE pixels, which would account for an uncertainty of ∼2 pixels in identifying both the start and end points of a ridge, and the position of successive crests. Ridge height and slope were extracted via an automated Python script from the topographic profiles for 42 of the 93 ridges within the spacing transects that exhibited well-defined troughs and crests (Figure 4c); the other 51 profiles exhibited ridge flanks that transitioned up-slope and down-slope without well-defined local minima. The ridges not included in height and slope measurements were similar in morphology and size to the 42 measured ridges, thus we consider population a small, but representative sampling of Glen Torridon ridge profiles. Although the height of a ridge can vary along its length, a measurement at the midpoint provides the maximum height of a ridge and a basis for standardized comparison between ridges. Ridge height was calculated by averaging the difference in elevation between the ridge crest and the local minima on either side of the ridge. The uncertainty associated with elevation measurements was considered to be the DEM vertical EP, estimated to be ±0.1 m. Ridge slope was measured by fitting a line through the start and end points that defined the middle half of each ridge flank (Figure 4c). Although this method assumed that the ridge flanks were planar over this section, which was not always the case, these slope estimates provided an objective basis for comparing the shape of ridge flanks. HiRISE stereopairs have slope errors of ∼1° at a 2 m baseline (Kirk & Herkehnhoff, 2010), which is near the minimum distance over which slope was measured along the flanks.

TARs in Glen Torridon, as well as a representative subset of active ripple crests in dark sand patches throughout Glen Torridon, were traced in ArcGIS to determine their orientation relative to the ridges. The generic term TAR is used in this paper to refer to meter- to decameter-long, bright, apparently symmetrical bedforms observed only in orbiter data. Where rover observations allow for interpretation of these features as megaripples, they are referred to as such, but we do not assume that all TARs observed in orbiter images are megaripples.

Few yardangs are present in the immediate vicinity of Glen Torridon, so streamlined hills further up-slope and south of Glen Torridon were included in the survey. This study's examination of TARs and active ripples is restricted to the immediate Glen Torridon region since the orientation of these features is strongly susceptible to local wind regimes, local topographic control, and changes on relatively short timescales. Ripple and TAR orientation is also known to vary widely throughout Gale crater (Day & Kocurek, 2016). Average ridge length, elevation, spacing, orientation, height, and slope and average TAR length and orientation are reported below and in Table 1 with an uncertainty of one standard deviation of the averaged values.

Thermal inertia values for the Glen Torridon ridge-bearing terrain and surrounding area (Christian et al., 2021) were extracted using Discrete Ordinate Radiative Transfer-based modeling according to the methods of Christian et al. (2022) from hyperspectral measurements from the CRISM (Murchie et al., 2007) instrument onboard MRO.

Table 1
Glen Torridon Bedrock Ridge and Transverse Aeolian Ridge (TAR) Morphology Statistics

	n	Min	Max	Average (±1 standard deviation)
Ridge length: All	1255	3 ± 1 m	206 ± 1 m	30 ± 19 m
Ridge length: Jura/Pettegrove Point	923	3 ± 1 m	206 ± 1 m	30 ± 20 m
Ridge length: Knockfarril Hill	265	7 ± 1 m	109 ± 1 m	30 ± 17 m
Ridge length: Glasgow	67	9 ± 1 m	103 ± 1 m	36 ± 19 m
Elevation range of individual ridges	1255	0.0 ± 0.1 m	14.0 ± 0.1 m	2.2 ± 1.7
Ridge spacing: All	93	7 ± 1 m	105 ± 1 m	28 ± 19 m
Ridge spacing: Jura/Pettegrove Point	56	8 ± 1 m	105 ± 1 m	30 ± 21 m
Transect 1	8	9 ± 1 m	100 ± 1 m	37 ± 33 m
Transect 2	5	8 ± 1 m	39 ± 1 m	25 ± 14 m
Transect 3	14	10 ± 1 m	39 ± 1 m	18 ± 7 m
Transect 4	12	13 ± 1 m	105 ± 1 m	35 ± 27 m
Transect 5	15	12 ± 1 m	81 ± 1 m	35 ± 19 m
Transect 6	3	14 ± 1 m	32 ± 1 m	21 ± 9 m
Ridge spacing: Knockfarril Hill	30	7 ± 1 m	60 ± 1 m	24 ± 14 m
Transect 1	7	13 ± 1 m	60 ± 1 m	31 ± 18 m
Transect 2	7	10 ± 1 m	22 ± 1 m	15 ± 4 m
Transect 3	6	11 ± 1 m	49 ± 1 m	26 ± 14 m
Transect 4	9	7 ± 1 m	44 ± 1 m	23 ± 12 m
Ridge spacing: Glasgow	7	16 ± 1 m	56 ± 1 m	37 ± 15 m
Transect 1	3	28 ± 1 m	56 ± 1 m	38 ± 20 m
Transect 2	5	16 ± 1 m	51 ± 1 m	35 ± 15 m
Ridge Orientation: All	1255	333°/153°	64°/244°	18°/198° ± 12°
Ridge Orientation: Jura/Pettegrove Point	923	333°/153°	64°/244°	18°/198° ± 11°
Ridge Orientation: Knockfarril Hill	265	337°/157°	50°/230°	18°/198° ± 13°
Ridge Orientation: Glasgow	67	337°/157°	56°/236°	22°/202° ± 16°
Leading Height (NW-facing flank): All		0.0 ± 0.1 m	4.3 ± 0.1 m	0.9 ± 0.9 m
Trailing Height (SE-facing flank): All		0.0 ± 0.1 m	2.4 ± 0.1 m	0.4 ± 0.5 m
Height (average of leading and trailing height): All		0.0 ± 0.1 m	3.3 ± 0.1 m	0.6 ± 0.7 m
Leading Slope (NW-facing flank): All		0° ± 1°	14° ± 1°	6° ± 4°
Trailing Slope (SE-facing flank): All		0° ± 1°	9° ± 1°	2° ± 2°
TAR Length: All	506	4 ± 1 m	34 ± 1 m	11 ± 5 m
TAR Orientation: All	506	18/°198°	158°/338°	120°/300° ± 13°

This method uses a neural network approach to model temperature from CRISM along-track oversampled observations at a resolution of 12 m/pixel, separating out the thermal and reflected components of radiance over the entire 2.9–3.7 micron wavelength range and fitting the thermal component to a black body (He et al., 2022). Temperatures are then used to estimate apparent thermal inertia (ATI) using the 1-D surface-atmosphere thermal model (Vasavada et al., 2017). ATI was averaged for the Glen Torridon Jura, Knockfarril Hill, and Glasgow members within the map area of Fedo et al. (2021) (Figure 5, Table 2). ATI average values were also calculated for the VRR Jura member and for the Murray formation north of VRR (Figure 5).

Rover images of the Glen Torridon ridges were examined for several purposes: (a) characterization of ridge morphology, bedrock, and related surface clasts, (b) comparison between ridges and modern aeolian features, and (c) evaluation of stratigraphic relationships between ridges and outcrops throughout the region. Images were acquired by the Curiosity rover's Mast Cameras (Mastcams; Bell et al., 2017; Malin et al., 2017) and Mars

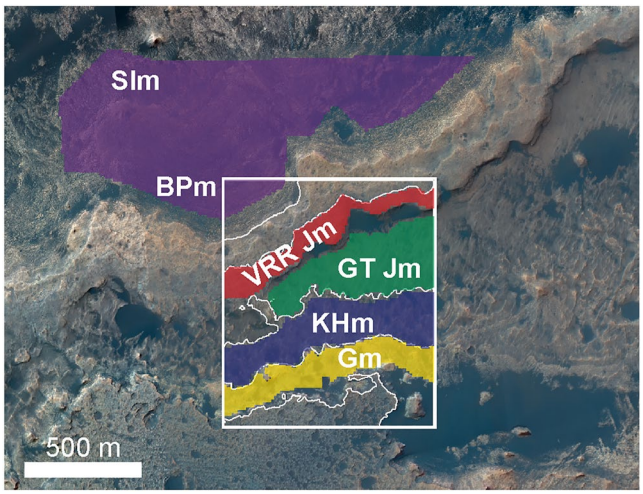

Figure 5. Areas over which the thermal inertia values reported in Table 2 were averaged. The center coordinate (lat, lon) of the area shown is −4.7257, 137.3852. North is up.

Descent Imager (MARDI; Malin et al., 2017). Mastcam consists of two color cameras of different focal lengths (34 and 100 mm) that are mounted in parallel on the pointable remote-sensing mast. MARDI is fixed to the body of the rover behind the left-front wheel, and points vertically downward at the surface. Color mosaics from the 34 (M-34) and 100 (M-100) mm fixed-focal-length Mastcams were used to characterize the bedrock and clasts comprising the Glen Torridon ridges. At a 2-m distance, the M-34 and M-100 cameras can achieve resolutions of 440 μm/pixel and ~150 μm/pixel, respectively, and MARDI has a resolution of ~1 mm at the surface (Malin et al., 2017). Mastcam mosaics were reprocessed as 24-bit (8-bits per color channel R [red], G [green], and B [blue]) color PNGs and re-registered, if needed, to remove mosaicking artifacts. Reprocessing involved radiometric calibration including flat fielding, dark current noise mitigation, bad pixel and line repair, Zhang-Wu Bayer Color Filter interpolation, color correction by white balancing, stretching for contrast and brightness adjustment, light spatial frequency adjustment, and additional gray balancing (Malin et al., 2017). Mastcam images were perspective projected.

Bulk geochemistry of clasts and bedrock on the crests, flanks, and troughs of ridges within Glen Torridon was measured by Curiosity's Alpha Particle X-ray Spectrometer (APXS; Gellert et al., 2015) between sols 2308 and 2928. Five targets were acquired in the GT Jura member: "Brent" (pebbles at a ridge crest), "Emerald_RP" (large pebble on ridge flank), "Almond_raster1" (small pebble in a ridge trough), "Iapetus" (bedrock in a ridge trough), and "Urr" (bedrock below ridge cap). Eight targets were acquired in the GT Knockfarril Hill mb: five targets in bedrock capping the ridges ("Calgary Bay," "Balnakettle," "Beauly_DRT," "Stack of Glencoul," and "Nedd") and three targets in bedrock on ridge flanks ("Orkney," "Blawhorn," and "Gorgie,"). Two pebbles on the flanks of ridges in the Glasgow mb were analyzed ("Racahn_TH" and "Garth Ness"). Observations on or near ridges were compared to all other non-ridge targets within GT Jura, Knockfarril Hill, and Glasgow members. All APXS data shown in this paper was sourced from O'Connell-Cooper et al. (2021).

Since the surfaces of most bedrock ridges within Glen Torridon are covered in small clasts (Khan et al., 2021), no drill samples were acquired of the bedrock directly on or within the ridges. However, relative strengths of ridge-bearing bedrock within the Glen Torridon Jura, Knockfarril Hill, and Glasgow members, were estimated based on the drilling parameters from nine drill samples acquired in bedrock adjacent or nearby to ridges. These qualitative estimates are based on the mode (rotary vs. percussive) and intensity level of drilling (Voice Coil Level, VCL) required to achieve the 40 mm minimum drill sample depth as in Peters et al. (2018). Any inferences about rock strength for the ridges extracted from Curiosity drill samples may be biased toward stronger, more resistant and better exposed drillable bedrock compared to that comprising the ridges.

Ridges were also characterized using rover mobility data acquired during several traverses over ridge crests or up ridge flanks. Elevation and slope as a function of traverse distance was calculated from Navcam stereo data (Maki et al., 2012), rover tilt was estimated from the rover's inertial measurement unit, and slip was estimated by comparing real drive distance estimated from Hazcam stereo data (Maki et al., 2012) with commanded drive distance.

Table 2
Apparent Thermal Inertia for Ridge- and Non-Ridge-Bearing Bedrock in and Near Glen Torridon

Color	Unit	ATI (±1 standard deviation)	Pixel count
Red	VRR Jura	356 ± 66	529
Green	GT Jura	296 ± 44	1036
Blue	Knockfarril Hill	294 ± 47	1076
Yellow	Glasgow	306 ± 78	720

The orientation of Glen Torridon ridges was compared against outputs from the Mars Weather Research and Forecasting (MarsWRF) model (Newman, 2022). The MarsWRF model has been used to simulate the atmospheric circulation inside Gale crater to compare with MSL Rover Environmental Monitoring Station (REMS) wind measurements (Newman et al., 2017) and to assist in interpreting observations of dust devils (Newman et al., 2019) and aeolian-driven surface changes (Baker, Lapotre, Minitti et al., 2018; Baker, Newman, et al., 2018; Baker et al., 2022). The output used in this work comes from the "vertical grid B" simulations described in Newman et al. (2017), which provide the best match to observed winds and aeolian

features. For Gale crater modeling, MarsWRF is run as a global model with nested higher-resolution domains that gradually increase the model's horizontal resolution over smaller and smaller areas, finally providing output at ~400 m grid spacing over the NW quadrant of the crater. The version of MarsWRF used here includes the treatment of radiative transfer in Mars's dusty CO_2 atmosphere, the seasonal CO_2 cycle, subsurface-surface-atmosphere exchange of heat and momentum, and vertical mixing of heat and momentum, with surface properties (topography, roughness, albedo, etc.) based on orbital datasets and the seasonally evolving, non-dust-storm "Mars Climate Database" dust distribution imposed (see Richardson et al., 2007 for more details).

The model outputs minute-by-minute predictions of surface friction velocity, u_*, and atmospheric density at 1.5 m, ρ, for 7 sols at each of 12 periods, which are equally spaced in planetocentric solar longitude (L_s) through the martian year. For each output, the surface wind stress, τ, is found from $\tau = \rho u_*^2$. We then adjusted the contribution of each period to account for the varying number of sols Mars spends around each period over its orbit, before producing wind stress roses, which thus represent the total wind stress and direction over a non-dust-storm Mars year.

4. Results

4.1. Orbiter Observations

4.1.1. Spatial and Stratigraphic Distribution

Ridges were mapped south of VRR, and occur over a lateral E-W distance of ~8 km, an area of ~2.6 km^2, and an elevation range of ~160 m, from −4,080 to −4,240 m, along the northwest flank of Mount Sharp (Figures 1a and 1b). Ridges are less common to the east and the west of Glen Torridon as both VRR and the Glen Torridon trough become less well-defined. The densest concentration of ridges occurs just south of VRR, midway along the lateral extent of Glen Torridon, and ridges typically occur in areas that appear relatively dark and smooth in HiRISE images (Figures 1 and 6). Much of this area has been mapped as GT Jura member (Fedo et al., 2021). However, because the eastward extension of the Pettegrove Point-Jura member contact has not yet been mapped with high confidence, there is a possibility that Pettegrove Point is exposed in the eastern part of Glen Torridon, and that some of the ridges occur within this member interval. The occurrence of ridges drops off steeply within the Glasgow member, with only rare occurrences of ridges present within this interval. No ridges were observed within the VRR Jura or VRR Pettegrove Point members exposures. Ridges also occur within the Knockfarril Hill member, which overlies the Jura member, and several ridges are observed to span the Jura-Knockfarril Hill member transition.

4.1.2. Ridge Characteristics

Crests of the Glen Torridon ridges are approximately aligned (Figure 6a), but slight sinuosity along crests is common (Figure 6b). Seven small impact craters disrupting ridge crests were identified throughout the ~2.6 km^2 ridge-bearing Glen Torridon area (e.g., Figure 6c). Two of these craters are between 3 and 4 m in diameter, 4 are between 7 and 10 m in diameter, and the largest is 14 m diameter. The ridges are relatively bright compared to modern aeolian ripple fields (e.g., Figure 6b), slightly darker than TARs observed throughout Glen Torridon (e.g., Figures 6c and 6d), with minimal to no tonal distinction between the ridges and inter-ridge areas. Exceptions to this include ridges that appear darker, smoother, and devoid of fractures compared to nearby exposures of resistant bedrock, although some ridges cross-cut resistant, fractured bedrock exposures and exhibit the tone, textures, and fractures of that bedrock (e.g., Figure 6d). This is most common in the Knockfarril Hill member. Some ridges within the Glen Torridon region exhibit y- or tuning-fork-shaped bifurcations (Figure 7). These bifurcated ridges are generally oriented such that the branches point downslope to the northeast (Figure 7).

4.1.3. Morphology

Ridge morphology measurements are summarized in Table 1 and Figure 8. Ridge length ranges from 3 ± 1 to 206 ± 1 m, with an average ridge length of 30 ± 19 m calculated from 1255 ridges (Figure 8a, Table 1). Average ridge length is consistent across the different members in which ridges are found. The maximum elevation range spanned end-to-end by any individual ridge is 14.0 ± 0.1 m, but the average change in elevation is 2.2 ± 1.7 m (Figure 8b, Table 1). Average ridge spacing calculated from all measured transects is 28 ± 19 m, with average spacing ranging from ~18 to 40 m for individual transects, with no systematic trends within or between transects measured within different members.

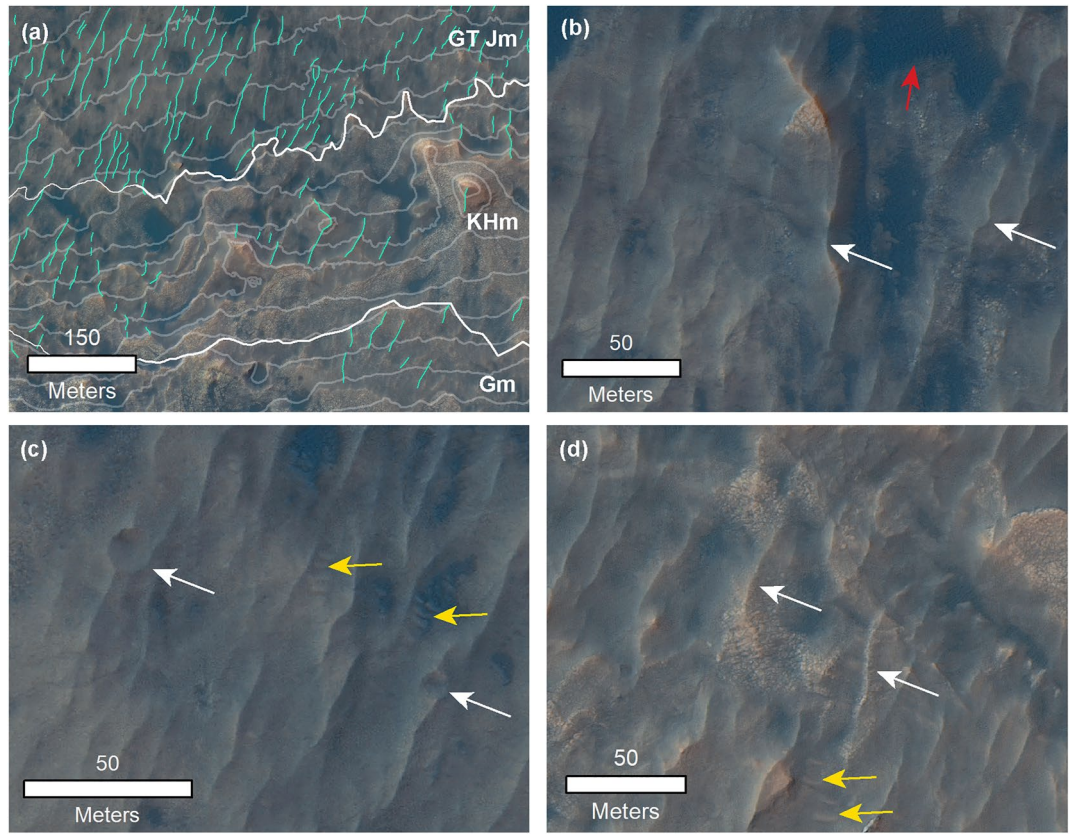

Figure 6. Characteristics of the Glen Torridon ridges observed in color High Resolution Imaging Science Experiment (HiRISE) images. North is up for all images; illumination from the left. (a) Ridges (green) within each of the members of the Glen Torridon region oriented nearly orthogonal to 5 m elevation contours (shown in gray). The center coordinate (lat, lon) of the area shown is −4.7293, 137.3962. HiRISE image ID: ESP_039280_1755, ESP_022111_1755. Member contacts annotated in white. (b) Slight sinuosity within Glen Torridon ridges annotated with white arrows. Red arrow points to dark aeolian sand. The center coordinate (lat, lon) of the area shown is −4.7119, 137.4199. HiRISE image ID: ESP_057108_1750. (c) Craters disrupting ridge crests (white arrows). Yellow arrows point to bright transverse aeolian ridges (TARs). The center coordinate (lat, lon) of the area shown is −4.7123, 137.4156. HiRISE image ID: ESP_037117_1755. (d) Example ridges in fractured, light-toned bedrock of the Knockfarril Hill member. Yellow arrows point to TARs. The center coordinate (lat, lon) of the area shown is −4.7255, 137.4032. HiRISE image ID: ESP_037117_1755.

Ninety-three topographic profiles were extracted across the mid-points of ridges within the transects spanning the Glen Torridon Jura, Knockfarril Hill, and Glasgow members (e.g., Figure 4c), of which 42 were measured for ridge height and ridge flank slope (Figures 8d and 8e, Table 1). Ridge heights up to 3.3 ± 0.1 m were measured, but most are no more than 1 m in height, with many approaching the sub-meter vertical resolution limits of the DTM (Figure 8d, Table 1). Most ridges are asymmetric in profile; 33 of the 42 measured ridges exhibit downslope, north-west facing troughs that are about a meter deeper than the upslope (e.g., Figure 4c), south-east facing trough. The northwest-facing ridge flanks are, on average, steeper (average slope of 6° ± 4°) than the southeast-facing ridge flanks (average slope of 2° ± 2°). This trend is also observed within individual ridges. This asymmetry is most extreme in the few instances throughout Glen Torridon where ridge orientation is similar to the expected strike of bedding. At these few locations, the ridges form a series of upslope benches, suggesting an influence of internal bedding on ridge morphology.

The Glen Torridon ridges are oriented very consistently NE-SW, with an average orientation (reported with an 180° ambiguity) for all ridges of 18°/198° ± 12° (Figure 9a, Table 1). With only a few exceptions including the benches mentioned above, the orientation of the Glen Torridon ridges is consistently at an ~60° angle to local elevation contours (Figure 6a). In HiRISE images, stratification is not observed to cross-cut the ridges since much of the Jura/Pettegrove Point appears massive throughout Glen Torridon. However, the orientation of the ridges

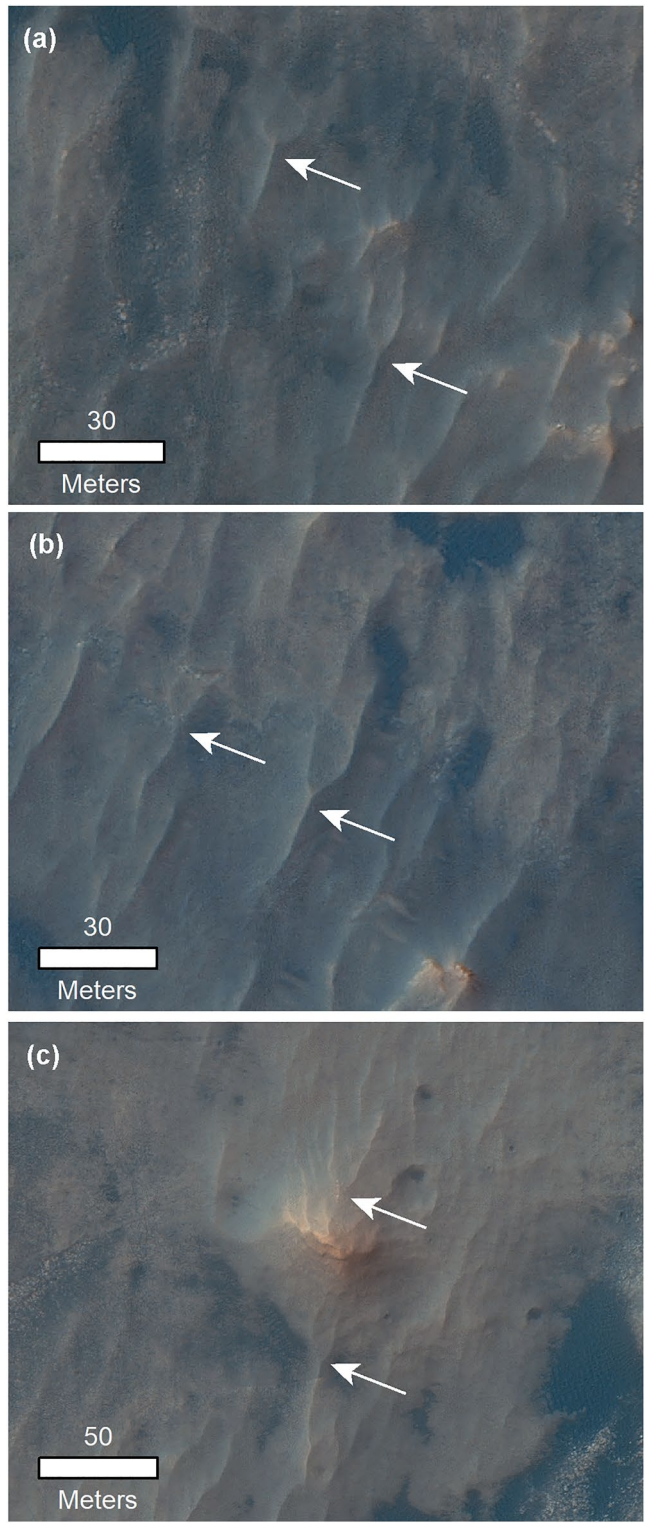

Figure 7. Color High Resolution Imaging Science Experiment (HiRISE) images showing examples of bifurcated ridges (white arrows) in Glen Torridon. North is up, illumination from the left. (a and b) Example y-junction ridge bifurcations. The center coordinate (lat, lon) of the area shown in panel (a) is −4.7256, 137.3959. HiRISE image ID: ESP_022111_1755. The center coordinate (lat, lon) of the area shown in panel (b) is −4.7147, 137.4189. HiRISE image ID: ESP_037117_1755. (c) Bifurcated ridges north and south of a small mound within the Glen Torridon region. The center coordinate (lat, lon) of the area shown is −4.7138, 137.4072. HiRISE image ID: ESP_037117_1755.

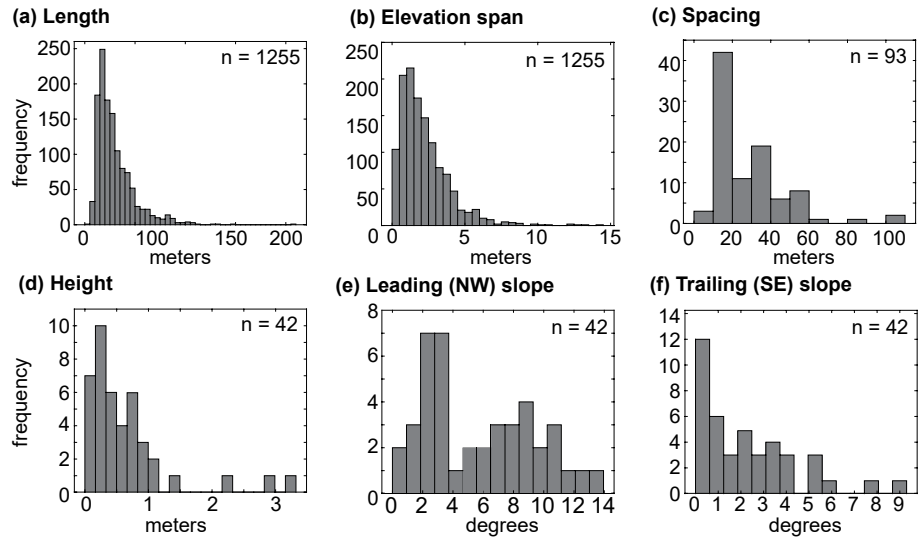

Figure 8. Histograms of ridge morphologic characteristics. (a) Ridge length, (b) elevation range spanned by the start and end of each ridge, (c) spacing between all ridges measured along the transects in Figure 2, (d) ridge height, (e) leading (NW) slope, and (f) trailing (SE) slope of 42 representative ridges exhibiting well defined crests and upslope and downslope troughs.

appears to be discordant offset to the strike of layering in VRR, Knockfarril Hill, and other overlying units that can be resolved in HiRISE images (Figure 1).

4.1.4. Relationship to Other Aeolian Features Throughout and Around Glen Torridon

Glen Torridon is host to two main classes of constructional aeolian bedforms observable in HiRISE images: bright TARs (e.g., Figure 10a) and fields of dark ripples (e.g., Figure 10b). TARs occur sparsely throughout the ridge-bearing areas of Glen Torridon, and are a brighter than adjacent sand and bedrock (Figure 10a). TARs are not common in the GT Jura/Pettegrove Point interval, but some do occur along the southern edge of VRR. TARs are more common throughout the Knockfarril Hill member, in which they commonly occur as series of parallel, aligned features in between the ridges (Figure 10a). Measurements of 506 TARs identified in HiRISE images throughout the Glen Torridon region reveal that they range from ~4 to 35 ± 1 m in length, with an average length of ~11 ± 5 m (Table 1). TARs are oriented consistently NW-SE throughout the study area—nearly orthogonal to the ridges—with an average orientation of 120°/300° (Figure 9b). The Glen Torridon TARs, which are interpreted to form transverse to the dominant wind direction and are presumed to be inactive given their bright dust cover, would suggest a NE or SW formative wind direction.

Patches of dark, rippled sand in Glen Torridon occur in some local topographic lows and along the southern base of VRR. These dark sand deposits are active seasonally around the time of planet perihelion (Sullivan, Baker, et al., 2020), similar to dark sand deposits elsewhere at Gale crater (Baker, Lapotre, Minitti et al., 2018; Baker, Newman, et al., 2018; Bridges et al., 2017). Crests of the largest ripples within the dark sand deposits are most commonly oriented NNW-SSE, with substantial variation depending on local topographic setting (e.g., Figure 10b). Cross-sectional asymmetries of the largest dark sand ripples indicate net ripple migration is approximately WSW (e.g., Figure 10b).

The Glen Torridon ridges are oriented approximately orthogonal to the dominant trend of linear ridges of unknown origin observed in the Stimson formation on the top surface of the "Greenheugh" pediment (Anderson & Bell, 2010; Kronyak et al., 2019), which are oriented E-W (100°/280°). The orientation of aeolian bedforms observed within Stimson formation outcrops capping the Greenheugh pediment supports paleowinds from north to south (Banham, Gupta, Bryk, et al., 2021). The orientation of aeolian erosional landforms including scour lines across the Greenheugh pediment surface and streamlined, elongate hills and mounds upslope from Glen Torridon are oriented generally N-S, mostly commonly ranging from NW/SE to NE/SW (Figure 10c). Some of these landforms, but not most, are aligned with the ridges (Figure 10c).

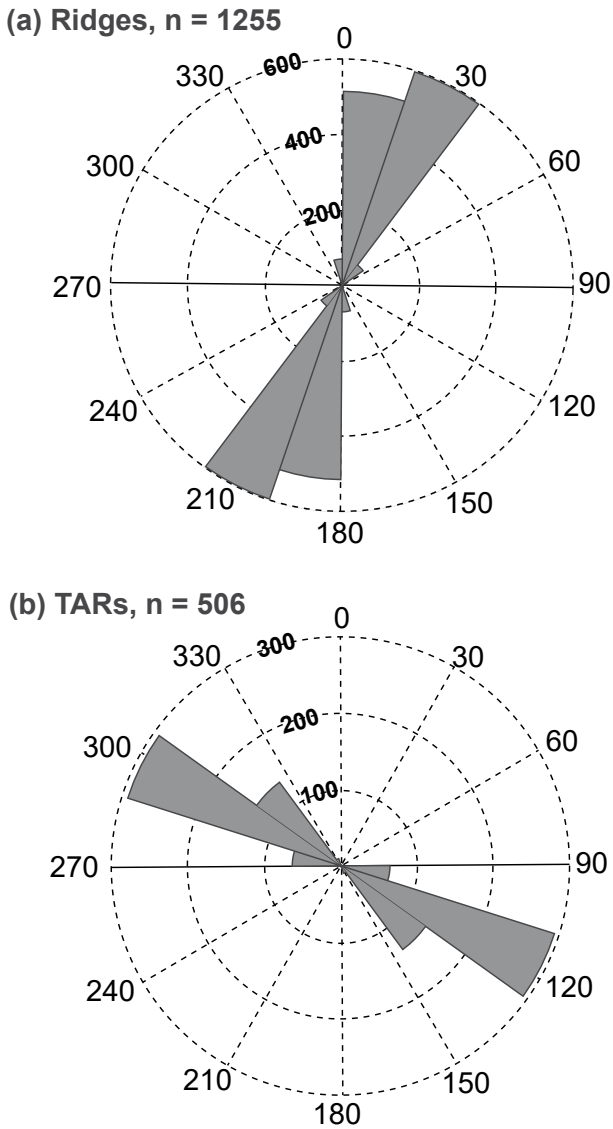

Figure 9. Polar histogram of crest orientation for Glen Torridon (a) ridges and (b) transverse aeolian ridges (TARs). TAR crestline orientations show a ~90° offset in orientation relative to the ridges. Crest orientation is plotted with an 180° ambiguity in wind direction.

4.1.5. Comparison Between Glen Torridon Ridges and MarsWRF Model Outputs

MarsWRF model outputs show that modern winds blowing to the SW, WSW, and SSW are most common within the region of Mount Sharp, including Glen Torridon, outlined in Figure 11a. Preferred wind directions shift toward the SSW moving E and S across the region. The strongest wind stresses are typically found in less common winds to the S (i.e., Figure 11b), even less common winds to the W, and rare winds to the E. Of the most frequently occurring winds, those to the SSW are strongest. The Glen Torridon ridges (Figure 9a) appear well aligned with the most common wind directions and the strongest wind stresses output by the MarsWRF model. TARs measured throughout Glen Torridon (Figure 9b) are oriented approximately orthogonal to the most common MarsWRF wind orientations.

4.1.6. Orbiter Mineralogy and Thermal Inertia

CRISM data show that the Glen Torridon area exhibits absorptions suggestive of Fe-smectite (Fox et al., 2021; Fraeman et al., 2016; Milliken et al., 2010). Although both the occurrence of ridges and the depth of spectral absorptions attributed to hydration and Fe-smectite decrease to the south/up-section transitioning from Jura to Knockfarril Hill to Glasgow members, the occurrence of ridges and clays mapped in orbital data are not uniquely correlated. There are strata with spectral absorptions attributed to clays throughout Glen Torridon that do not contain ridges, and there are some ridges that occur outside the regions identified by Fox et al. (2021) as smectite-bearing in orbital data.

The ATI of the ridge-bearing members of Glen Torridon and terrains surrounding this area can be found in Table 2 (Figure 5). The ridge-bearing GT Jura and Knockfarril Hill members exhibit the lowest ATI at 296 ± 44 (standard deviation) and 294 ± 47 J m^{-2} K^{-1} $s^{-½}$, respectively. The Glasgow member, in which ridges are rare, has an ATI of 306 ± 78, which, while higher than the GT Jura and Knockfarril Hill members, are all within recognized statistical uncertainty. For comparison, the VRR Jura member, located just north of the GT Jura exposure and which is devoid of ridges, has an ATI of 365 ± 66. The Murray formation exposed north of VRR, which also lacks ridges, has the lowest ATI for this area, with an average of 229 ± 23. Modeling of the CRISM-based thermal inertia by Christian et al. (2022) is consistent with mixtures of bedrock, regolith, and sand-sized grains within the ridge-bearing regions of Glen Torridon.

4.2. Curiosity Rover Observations

The Glen Torridon area observed in Curiosity rover mosaics is a rolling landscape of ridges with only rare exposures of bedrock (Figure 12a). Ridges and inter-ridge surfaces are most commonly covered by a mix of dust, sand-sized grains, and mm-to-cm scale pebbles and cobbles (Khan et al., 2021) (Figure 13c). In the vicinity of five ridges traversed by Curiosity within the Glen Torridon Jura interval, 10–25 mm clasts are common (Khan et al., 2021). Although bedrock exposures throughout northern Glen Torridon are sparse, ridges are sometimes capped by cross-bedded sandstone outcrops of the Knockfarril Hill member (Figures 12b, 13a and 14b). This relationship was first observed at the "Knockfarril Hill" outcrop, for which the Knockfarril Hill member is named, early in Curiosity's exploration of Glen Torridon (sols 2306–2309) (Figure 13). A similar relationship was observed again between sols 2439–2447 during Curiosity's ascent to the crest and capping outcrop of the "Teal" ridge, located near the transition between the Jura and Knockfarril Hill members between sols 2439–2447 (Figure 14). Some sandstone outcrops are aligned with the linear crest of the ridges they cap, as at the northern extent of the Knockfarril Hill namesake outcrop (Figure 13a), while elsewhere the capping sandstones locally

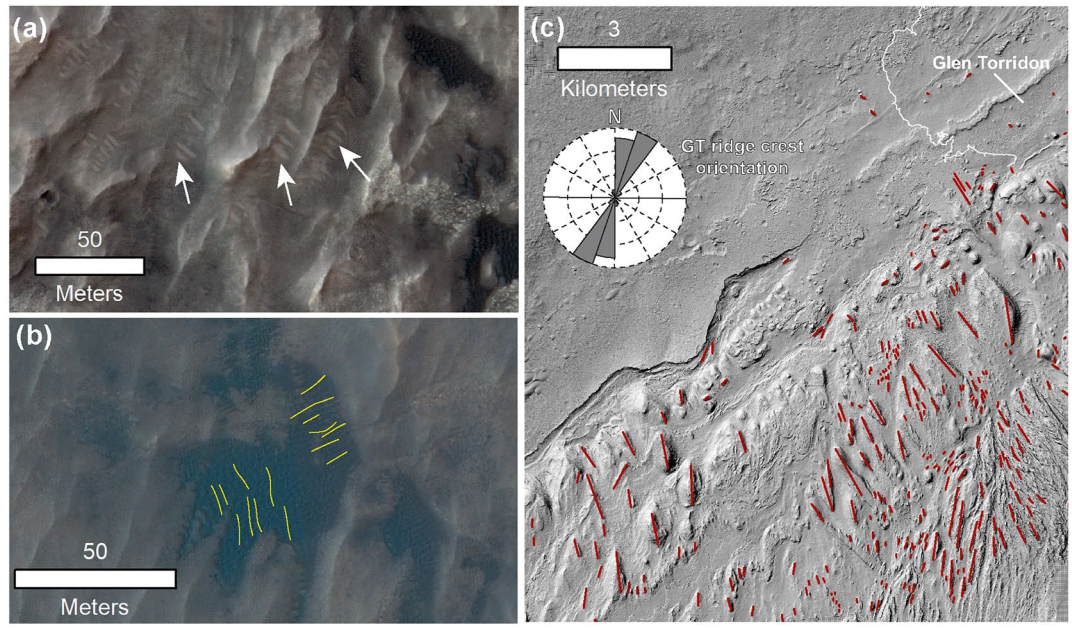

Figure 10. Orientation of other aeolian bedforms and landforms in and around Glen Torridon. North is up. North is up; illumination from the left for panels (a and b). (a) Transverse aeolian ridges (white arrows) oriented perpendicular to adjacent bedrock ridges. The center coordinate (lat, lon) of the area shown is −4.6955, 137.4440. High Resolution Imaging Science Experiment (HiRISE) image ID: ESP_028612_1755. (b) Representative orientation of ripple crests (yellow lines) in sand patches within Glen Torridon. The center coordinate (lat, lon) of the area shown is −4.7241, 137.3943. HiRISE image ID: 039280_1755. (c) Hill-shade derived from the HIRISE DEM mosaic showing the orientation of streamlined mounds on the NW slope of Mount Sharp (red). The orientation of the Glen Torridon ridges is shown in the inset polar histogram. The center coordinate (lat, lon) of the area shown is −4.4187, 137.3272.

exceed the width of the underlying ridge (i.e., southern end of the Knockfarril Hill outcrop, Figure 13b). Small (centimeter to decimeter-scale) exposures of rubbly bedrock are sparsely distributed on ridge flanks (Figure 14c). Coherent, well-preserved bedrock exposures are more extensive throughout the Knockfarril Hill than in the Jura/Pettegrove Point member of northern Glen Torridon, and ridges observed within the Knockfarril Hill interval are more likely to have coherent bedrock exposed at ridge crests and on flanks (i.e., "Rock Nab" ridge, Figures 12d and 12e).

Typically, there is very little local diversity in clast lithology on and near the ridges (Khan et al., 2021). Clasts on or near the ridges are uniform in tone, color, and texture, and are generally reflective of and consistent with the lithological properties of nearby bedrock outcrops (e.g., Figure 13). Clasts are uniformly very fine-grained, sometimes laminated, and are often characterized by pits and polygonal facets (Khan et al., 2021). Colors range from gray to reddish-purple, but locally clast color within any particular nearfield scene imaged by the rover varies little (Figure 14c). Given the predominance of pebbles and sand on ridge flanks, and the rarity of coherent bedrock exposures on many ridges, particularly those in northern Glen Torridon, resolving interior structure such as layering within the ridges is challenging, except within the occasional ridge-capping sandstone outcrops (i.e., Figure 14b).

4.2.1. Other Aeolian Features Observed by Curiosity

Seasonal sand migration at Glen Torridon is approximately WSW based on MSL observations of sandy wind tails extending WSW from obstacles, westward erosion of drill tailings piles, crest orientations and morphologies of the largest dark sand ripples, and orbital views showing a dark wind streak extending WSW from the "Sands of Forvie" ripple field (Sullivan, Baker, et al., 2020). A secondary wind direction, blowing approximately orthogonally and down-gradient from Aeolis Mons, is indicated by orientations and morphologies of smaller secondary ripples in troughs between the larger dark sand ripples (Sullivan, Baker, et al., 2020).

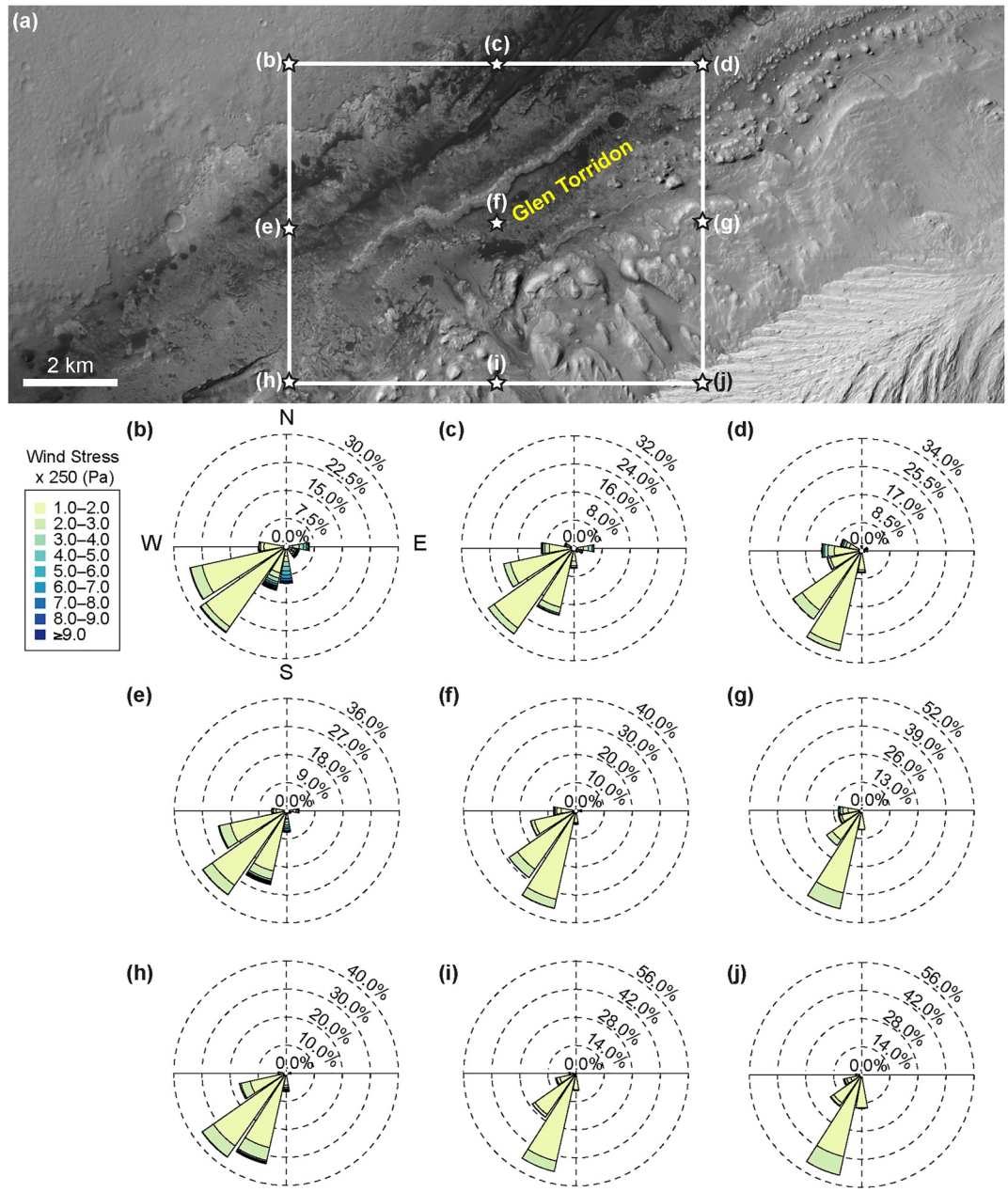

Figure 11. Rose diagrams showing frequency and wind stress magnitude of each direction toward which wind blows derived from the MarsWRF model over one Mars year for a grid covering a rectangular area (a) with its lower left corner at [−4.786, 137.321] and upper right corner at [−4.671, 137.469]. Units are wind stress × 250 in Pa. (b) Wind stress rose at [−4.671, 137.321], (c) wind stress rose at [4.671, 137.395], (d) wind stress rose at [−4.671, 137.469], (e) wind stress rose at [−4.728, 137.321], (f) wind stress rose at [−4.728, 137.395], (g) wind stress rose at [−4.728, 137.469], (h) wind stress rose at [−4.786, 137.321], (i) wind stress rose at [−4.786, 137.395], and (j) wind stress rose at [−4.786, 137.469].

Consistent with measurements of TARs throughout Glen Torridon, inactive megaripples observed by Curiosity along the rover's traverse through Glen Torridon generally have orientations orthogonal to the ridges, although some megaripples are observed parallel to the ridge crests (Sullivan, Baker, et al., 2020; e.g., Figure 13b). Megaripple crest morphologies are 180° ambiguous about whether their formative winds

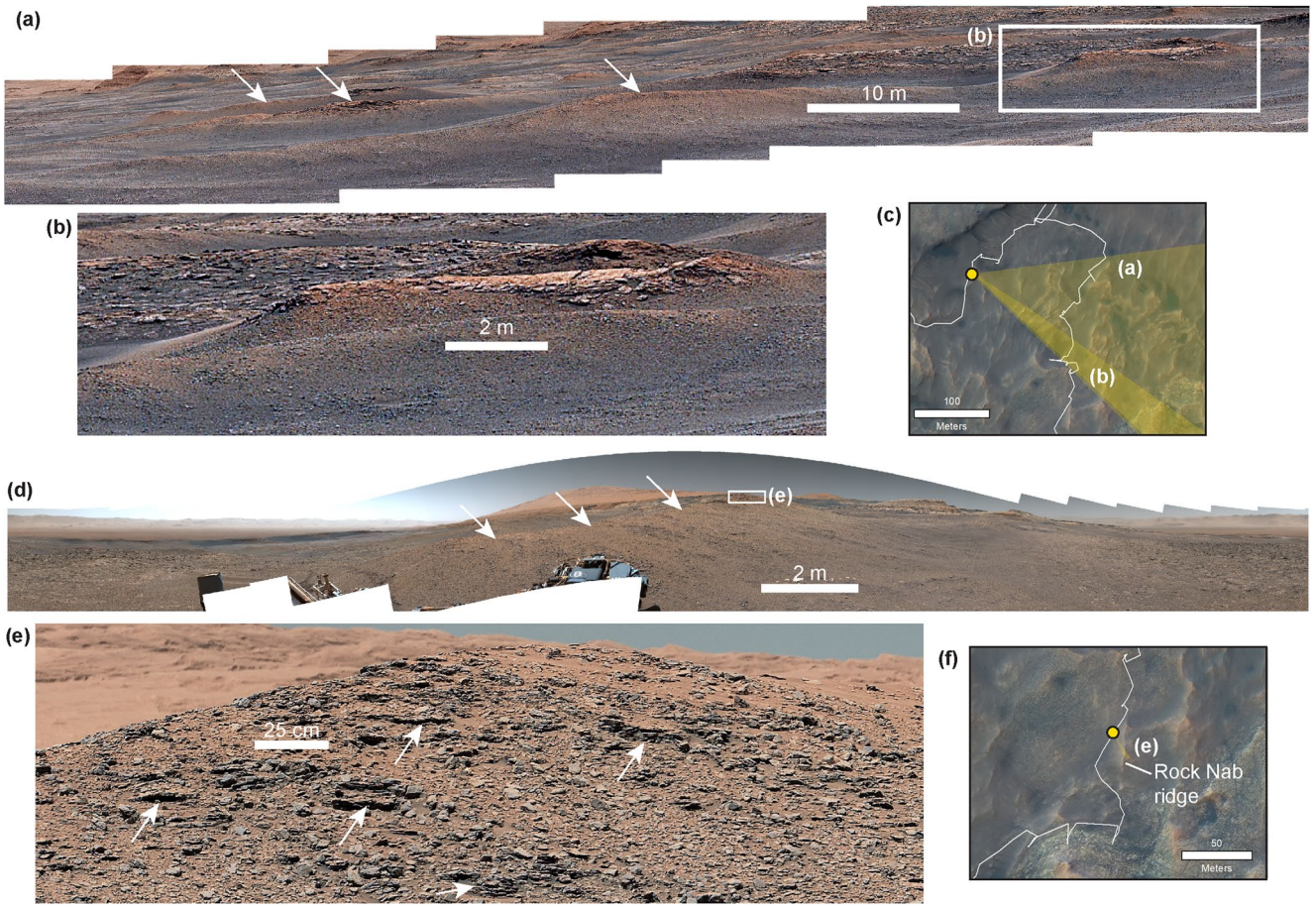

Figure 12. (a) Left-eye Mastcam mosaic looking to the ESE of Gillies Hill ridge acquired on sol 2320. White arrows point to other ridges in the background. (b) Capping Knockfarril Hill member sandstone on the Gillies Hill ridge in a left-eye Mastcam mosaic acquired on sol 2320. (c) High Resolution Imaging Science Experiment image showing the approximate viewshed of panels (a and b). The center coordinate (lat, lon) of the area shown is −4.7296, 137.3836. (d) Left-eye 360° Mastcam mosaic of the Rock Nab ridge in the Knockfarril Hill member acquired on sol 2560. White arrows point along the crest of the ridge; the white box shows the location of the outcrop shown in panel (e). (e) Close-up view of the bedrock comprising the Rock Nab ridge in a right-eye Mastcam mosaic acquired on sol 2564. (f) HiRISE image showing the approximate viewshed of panel (e). The 360° mosaic in panel (d) was also taken from this position. The center coordinate (lat, lon) of the area shown is −4.7315, 137.8535. Image credit for Mastcam images: NASA/Caltech-JPL/MSSS.

drove sand primarily to the SW, or to the NE, or in both directions at different times (Sullivan, Baker, et al., 2020).

4.2.2. Ridge Mineralogy and Elemental Geochemistry

During the rover's traverse through Glen Torridon, APXS was used to characterize loose clasts and bedrock in the troughs, on the flanks, and at the crest of several ridges. Clasts and bedrock on and near the ridges in the GT Jura member are in family with non-ridge Murray bedrock, and tend to exhibit compositions typical of either a high Mg, low K Murray class or low Mg, high K category (O'Connell-Cooper et al., 2021). Analyses of coherent bedrock and clasts cropping out at the crest or troughs of ridges in the Jura member fall within the low Mg/high K class (Figure 15). Knockfarril Hill sandstone cropping out at the crest of Teal ridge shows consistent high Mg/low K compositions (Figure 15), although other bedrock targets located on ridge flanks within the Knockfarril Hill member show compositions with lower to medium Mg with only slightly elevated to elevated K.

ChemCam results are consistent with the APXS analyses and show two compositionally distinct classes of bedrock and clast targets throughout Glen Torridon characterized primarily by high K/low Mg or low K/high Mg (Dehouck et al., 2022). Dehouck et al. (2022) observe similar enrichments in K_2O and SiO_2 for both "rubbly bedrock" within the Glen Torridon Jura and the abundant clasts throughout the area found in the troughs between ridges and on the flanks of the ridges themselves. This enrichment in K_2O may be due to the presence of the clay

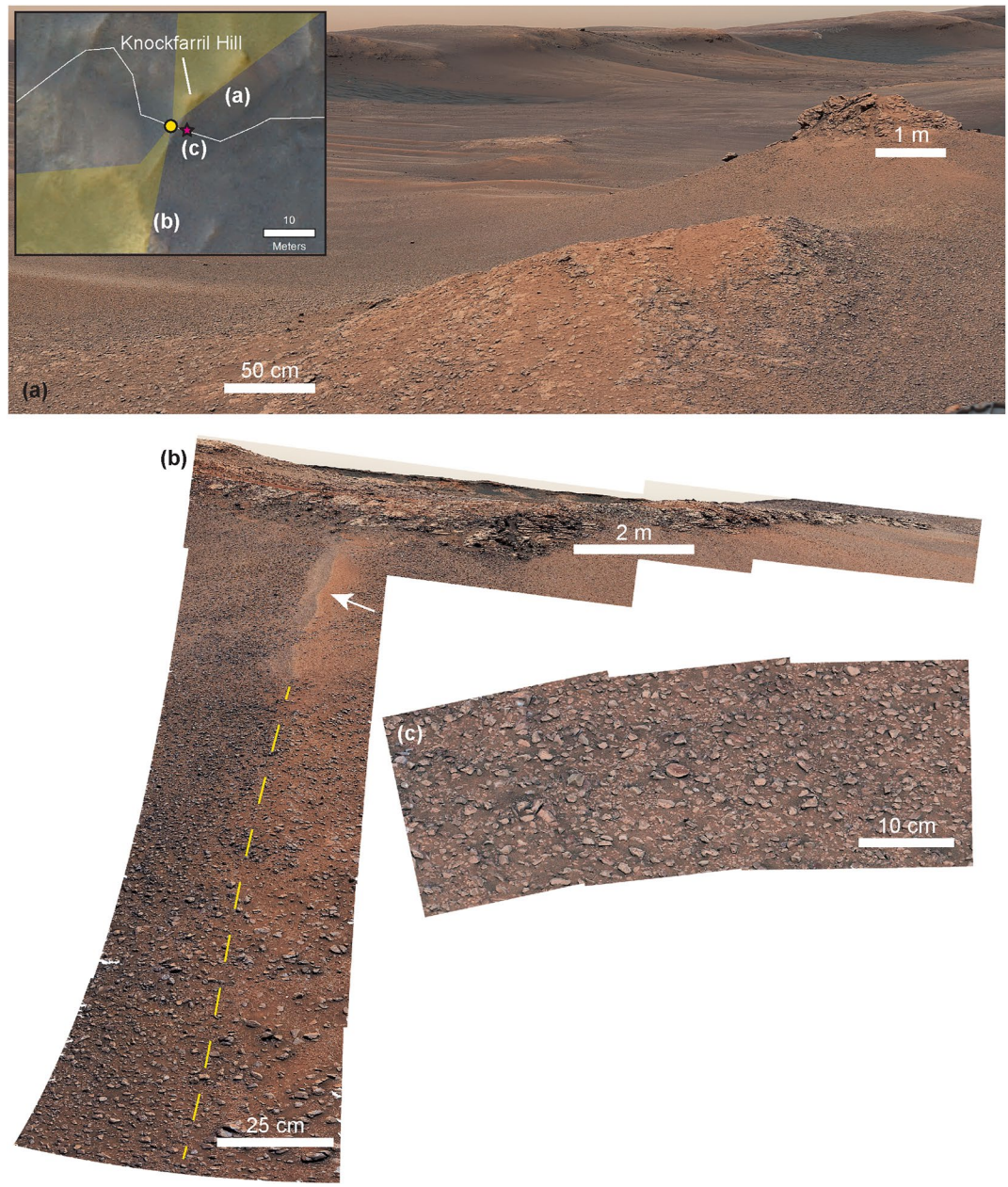

Figure 13. Views of the Knockfarril Hill ridge, the outcrop for which the Knockfarril Hill member was named, in Mastcam mosaics. (a) Capping sandstones of the Knockfarril Hill ridge in a Mastcam left-eye mosaic acquired on sol 2309; view is to the NNE. The center coordinate (lat, lon) of the inset area shown in High Resolution Imaging Science Experiment is −4.7293, 137.3801. (b) ~4 m-long megaripple (white arrow), as evidenced by its asymmetry and grain size, aligned with the crest of Knockfarril Hill ridge (yellow dashed line). Left-eye Mastcam mosaic acquired on sol 2309 looking SSW. (c) Right-eye Mastcam mosaic of the "Brent" target acquired on sol 2308 of the clast-covered flank of Knockfarril Hill ridge. Image credit: NASA/Caltech-JPL/MSSS.

mineral illite (Cousin et al., 2021). Coherent bedrock within the Glen Torridon Jura, likely what is represented in the "Aberlady" and "Kilmarie" drill samples, tends to show higher MgO and lower K_2O (Dehouck et al., 2022).

Although no Glen Torridon ridges were directly drilled by Curiosity, drill samples acquired from bedrock outcrops near the ridges provide the best approximation of ridge bedrock composition. CheMin (Chemistry and Mineralogy, Blake et al., 2012) instrument results from the 9 drill samples analyzed within the Glen Torridon Jura (Aberlady and Kilmarie), Knockfarril Hill ("Glen Etive 1 and 2," "Groken," "Mary Anning," and "Mary

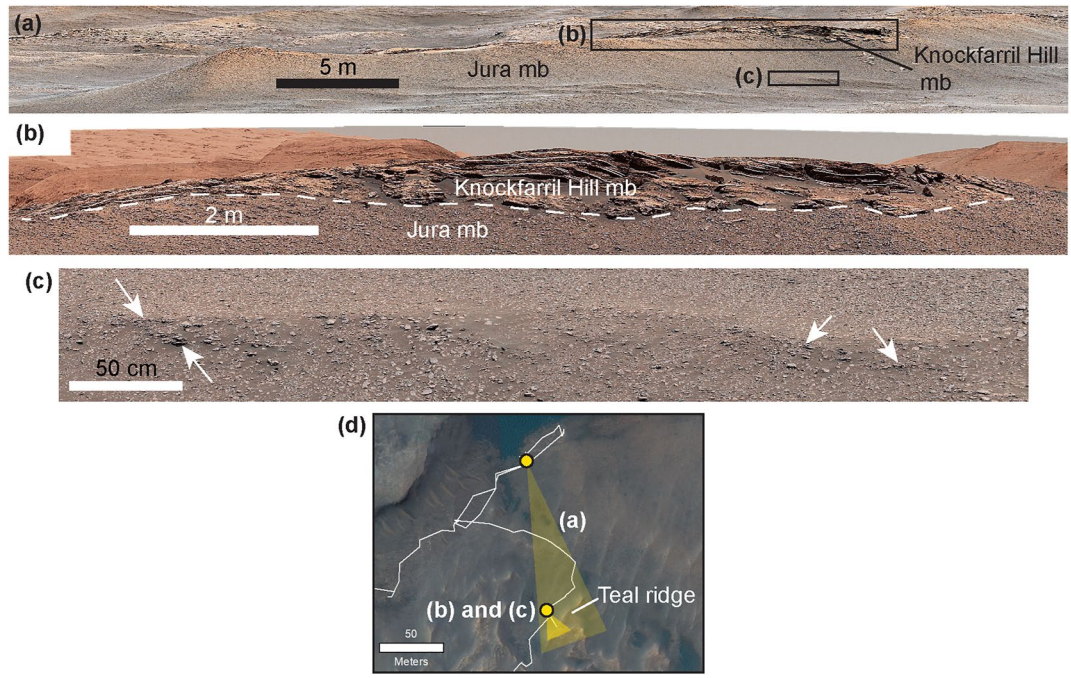

Figure 14. Views of Teal ridge observed with Mastcam. View is to the east. (a) Teal Ridge in a Mastcam right-eye mosaic acquired on sol 2365. Black boxes show the location of areas shown in panels (b and c). (b) Contact (white dashed line) between cross-bedded Knockfarril Hill member sandstone (cross-strata are traced in white) and underlying GT Jura member at the cap of Teal ridge in a Mastcam left-eye mosaic acquired on sol 2437. (c) Rubbly clasts, possibly eroding from in-place exposure, along the flank of Teal ridge in a Mastcam right-eye mosaic acquired on sol 2437. White arrows point to small in-place portions of the outcrop. Image credit: NASA/Caltech-JPL/MSSS. (d) Approximate viewsheds for the Mastcam mosaics displayed in panels (a–c). The center coordinate (lat, lon) of the area shown in High Resolution Imaging Science Experiment is −4.7274, 137.3837.

Anning 3"), and Glasgow members ("Hutton" and "Glasgow") show that this interval of Mount Sharp contains some of the most clay mineral-rich bedrock yet explored by Curiosity (Bristow et al., 2021; Thorpe et al., 2021). Clay content ranges from 23 to 34 wt. % smectite clay minerals (Bristow et al., 2021; Thorpe et al., 2021). For comparison, clay mineral content of the VRR drill samples is <15 wt. %. CheMin and Sample Analysis at Mars (Mahaffy et al., 2012) results reveal that the dominant smectite within these samples is consistent with an Fe-smectite similar to nontronite (McAdam et al., 2021; Thorpe et al., 2021). Although the Glen Torridon drill samples are generally compositionally similar, the Aberlady and Kilmarie drill samples show the first detection of Fe(II)-carbonate observed in Gale crater by Curiosity (Thorpe et al., 2021). Hematite abundance is relatively low (<2 wt. %) in the GT Jura and Knockfarril Hill member drill samples, but highest (~3–4 wt. %) in the Glasgow member drill samples (Bristow et al., 2019, 2021; Thorpe et al., 2021).

4.2.3. Rock Strength of Ridge-Bearing Bedrock

Parameters and inferred rock strength obtained from the 9 Glen Torridon drills (Figure 3) are shown in Table 3. Three of the Glen Torridon drills (Aberlady, Glen Etive 1, and Groken) were rotary only drills, suggesting low rock strength in family with the Telegraph Peak-Buckskin strength class of Peters et al. (2018) (<8 MPa; Table 3). The remaining Glen Torridon drills (Kilmarie, required some percussion, but no more than VCL 2. This is consistent with the Peters et al.'s (2018) Telegraph Peak-Buckskin-Mojave 2 strength class (<8–8.5 MPa; Table 3).

In comparison to the Glen Torridon bedrock drills, the Rock Hall drill sample acquired in non-ridge-bearing VRR Jura member bedrock used rotary only to start, then transitioned between VCL 1 through 4 for the remainder of drill operations. The bedrock drilled in the VRR Jura member is consistent, in a relative sense, with the (<8–12.5 MPa) Buckskin, Mojave 2, and Quela strength classes of Peters et al. (2018) (G. Peters, pers. comm.). A previous attempt to drill the target "Inverness" within the VRR Jura member on sol 2170 failed at only 6 mm depth at a max VCL of 5, suggestive of much stronger and harder bedrock than any observed within Glen Torridon.

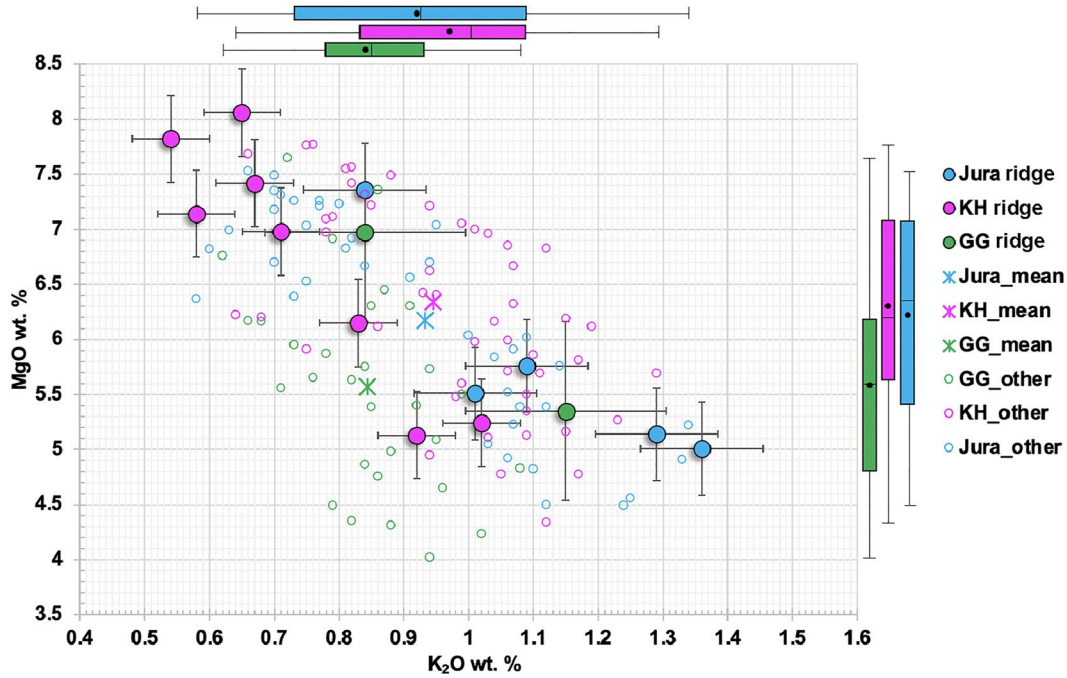

Figure 15. Plot of K versus Mg measured by APXS on and near the Glen Torridon ridges showing that ridge bedrock compositions are within the range of compositions observed for non-ridge bedrock within the Glen Torridon region. Ridge bedrock observations are shown in solid circles and plotted with average member composition (X symbol), and all other non-ridge measurements from those members (open circles). The colored boxes in the box and whisker plots represent the middle 50% of all member data; the black circle is the mean member composition, and the black line is the median. KH = Knockfarril Hill member. GG = Glasgow member. Data sourced from O'Connell-Cooper et al. (2021).

4.2.4. Ridge Characteristics Observed From Mobility Data

During its traverse through Glen Torridon, Curiosity drove over or near several ridges (Figures 3, 16, and 17). The sol 2306 and 2309 drives occurred shortly after Curiosity descended VRR into Glen Torridon, and included drives up the northwest-facing flank of the Knockfarril Hill ridge to the ridge crest (sol 2306) and down the southeast-facing flank (sol 2309) (Figure 16a). During the sol 2306 drive up-flank, Curiosity experienced ~2° to 12° tilts, consistent with ~5° to 11° slopes derived from a Navcam DEM (Figure 16c). The Navcam DEM elevation profile for the traverse shows a near-exponential shape with a steepening of the slope near the ridge crest (Figure 16c). During the descent of the southeast flank of the ridge on sol 2309 (Figure 16d), the rover experienced tilts between 4-9°.

A 16.4 m-long drive on sol 2439 advanced the rover up the northwest-facing flank of Teal ridge, located near the contact between the Jura and Knockfarril Hill members, over a surface of compact regolith to position Curiosity in front of Knockfarril Hill member sandstone cropping out at the ridge crest (Figure 17). During this drive, the rover experienced 5°–23° tilts (Figure 17d). Images of the sol 2439 rover tracks show relatively shallow wheel impressions in the regolith, indicating little sinkage during the traverse up the ridge (Figure 17b). This is further supported by the plot of slip versus tilt (Figure 17d), which follows a systematic trend of increasing slip with tilt, as would be expected on a relatively cohesive surface.

5. Discussion

5.1. Origin of the Glen Torridon Ridges

The 60° offset between ridge crests and the expected strike of bedding, the limited length of the ridges (typically 10s of meters), and the prevalence of bifurcations rule out an origin for the Glen Torridon ridges as either the erosional expression of bedding planes or as water-carved terraces. A glacial origin as eskers is ruled out by ridge morphology and the large number of closely spaced ridges throughout Glen Torridon, as well as rover

Table 3
Summary of Drill Parameters for Glen Torridon Drill Samples

Member	Drill sample	Sol acquired	Drill mode	VCL	Time at percussion level (s)	Likely strength class (Peters et al., 2018)	Strength
VRR Jura	Inverness	2170	Rotary-percussive	1	19.9	Oudam-Sebina-Marimba	12 to >18 MPa
				2	27.9		
				3	19.9		
				4	27.9		
				5	63.8		
VRR Jura	Rock Hall	2261	Rotary-percussive	1	95.6	Buckskin-Mojave 2-Quela	<8–12 MPa
				2	119.5		
				3	151.4		
				4	8.0		
GT Jura	Aberlady	2370	Rotary-only	–		Telegraph Peak-Buckskin	<8 MPa
	Kilmarie	2384	Rotary-percussive	1	127.5	Telegraph Peak-Buckskin-Mojave 2	<8–8.5 MPa
				2	75.7		
Knockfarril Hill	Glen Etive 1	2486	Rotary-only	–		Telegraph Peak-Buckskin	<8 MPa
	Glen Etive 2	2527	Rotary-percussive	1	143.4	Telegraph Peak-Buckskin-Mojave 2	<8–8.5 MPa
	Mary Anning 1	2838	Rotary-percussive	1	207.2	Telegraph Peak-Buckskin-Mojave 2	<8–8.5 MPa
				2	39.8		
	Mary Anning 3	2870	Rotary-percussive	1	99.6	Telegraph Peak-Buckskin-Mojave 2	<8–8.5 MPa
				2	63.8		
	Groken	2910	Rotary-only	–		Telegraph Peak-Buckskin	<8 MPa
Glasgow	Hutton	2668	Rotary-percussive	1	8.0	Telegraph Peak-Buckskin-Mojave 2	<8–8.5 MPa
	Glasgow	2754	Rotary-percussive	1	155.4	Telegraph Peak-Buckskin-Mojave 2	<8–8.5 MPa

observations of grain size, sorting, and clast homogeneity inconsistent with a glacial origin. Possible explanations for the Glen Torridon ridges are: (a) gravel-mantled, unconsolidated, constructional bedforms (Figure 18a), (b) exhumed, indurated paleobedforms (Figure 18b), (c) erosional ridges carved into the Glen Torridon bedrock by winds transverse to the ridges (Figure 18c), (d) erosional ridges carved transverse to the dominant wind direction, but with erosion occurring between unconsolidated or indurated bedforms armoring the bedrock (Figure 18d), or (e) erosional ridges carved into the Glen Torridon bedrock by winds parallel (Figure 18e) or oblique (Figure 18f) to the ridges.

Observations do not support an interpretation of the Glen Torridon ridges as modern, unconsolidated, constructional bedforms. Although the length and plan-view morphology of the Glen Torridon ridges is reminiscent of constructional aeolian bedforms such as megaripples or linear dunes, bedrock crops out within the Knockfarril Hill member ridges (Figure 12e) showing that they are lithified. Furthermore, capping sandstones like those observed at Knockfarril Hill (Figure 13a) and Teal (Figures 14a and 14b) ridges could not occur at ridge crests if the ridges were unconsolidated, modern bedforms. Mobility images show that the ridges are cohesive enough to prevent significant sinkage of the rover's wheels (e.g., Figure 17), which would not be expected if the bedforms were currently unconsolidated. Previous traverses onto and across unconsolidated bedforms at places such as Dingo Gap and Hidden Valley resulted in rover wheel tracks with sinkage up to ~30% of the 0.50 m wheel diameter (Arvidson et al., 2017). The pebbles and cobbles armoring the ridges are generally too large to have been reasonably transported by the wind (e.g., Figures 13c and 17c; Khan et al., 2021). Also, while some Glen Torridon ridges are symmetrical, most are asymmetrical with steeper downslope troughs. This morphology is inconsistent with megaripple, TAR (e.g., Berman et al., 2018, 2011; Geissler, 2014), or dune morphology. Finally, the Glen Torridon ridges are distinct in tone and are oriented orthogonally to the brighter, dustier coarse-grained TARs and megaripples observed throughout Glen Torridon (Figures 9 and 10a).

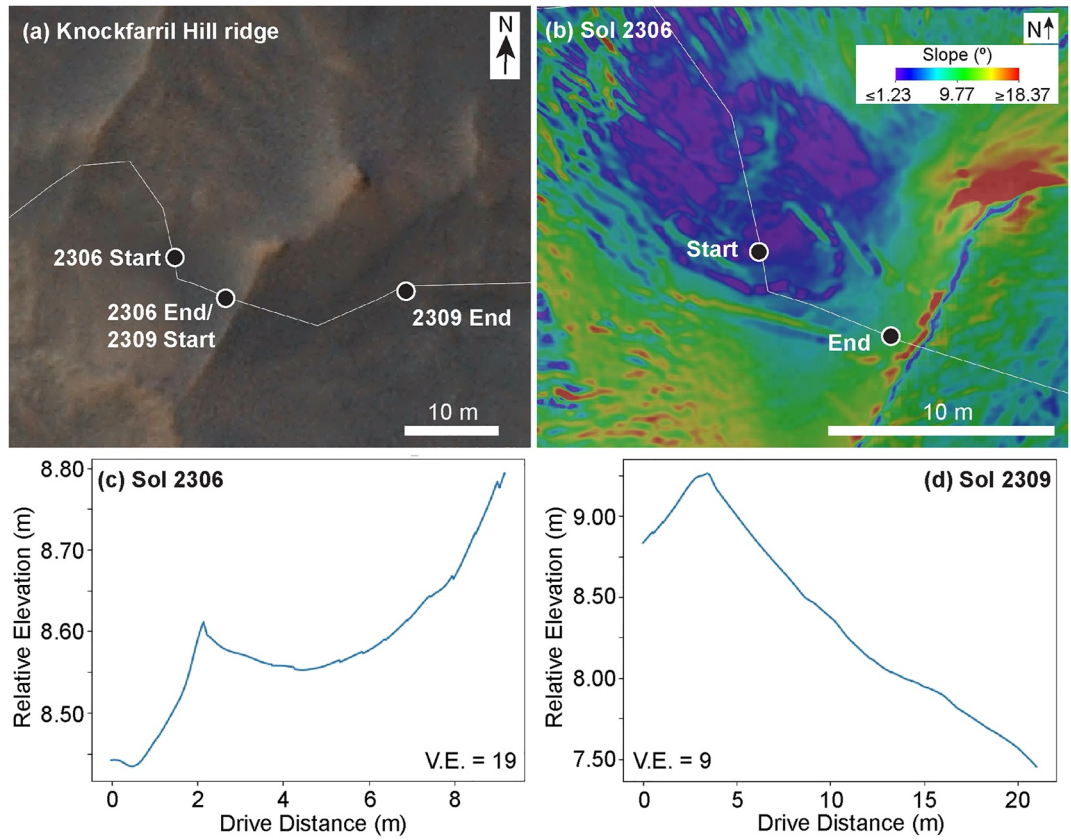

Figure 16. Mobility data from the Sol 2306 and 2309 drives up and down the namesake Knockfarril Hill ridge. (a) High Resolution Imaging Science Experiment (HiRISE) map showing the start and end of the sol 2306 and 2309 drives. The center coordinate (lat, lon) of the area shown is −4.7292, 137.3803. Illumination is from the left. HiRISE image ID: ESP_039280_1755. (b) Slope map derived from sol 2306 Navcam stereo data. North is up for panels (a and b). (c) Elevation profile for the sol 2306 drive extracted from the Navcam stereo data. Vertical exaggeration is 19. (d) Elevation profile for the sol 2309 drive extracted from the Navcam stereo data. Vertical exaggeration is 9.

It is also unlikely that the Glen Torridon ridges represent ancient lithified constructional bedforms or erosional features exhumed during the erosion of Mount Sharp (Figure 18b). The Glen Torridon ridges incorporate within them, and without distortion, the contacts of regional bedrock units (Figure 6a). Although the Glen Torridon ridges generally lack obvious internal structure and layering as observed in rover images, HiRISE images show that the ridges are consistently discordant with the orientation of bedding where it is exposed and traceable (Figure 1b). Yet the clasts that armor the ridges and bedrock observed within the ridges appear to be the same lithology and composition as bedrock exposed between the ridges (Figure 15). These observations are inconsistent with an origin as mobile aeolian bedforms that once migrated across ancient surfaces independent of their substrate, became indurated then subsequently buried, and are now partly exhumed.

The most likely explanation for the Glen Torridon ridges is that they are PBRs, bedrock ridges carved by the wind during the erosion of Mount Sharp, significantly post-dating the deposition of the bedrock units that are observed in and around the Glen Torridon area. Montgomery et al. (2012) first coined the term PBR to describe "megaripple forms eroded into cohesive substrate." These landforms exhibit decameter-scale spacing, an orientation discordant with local strata, and lack the streamlined shape often associated with yardangs (Montgomery et al., 2012). Montgomery et al. (2012) interpreted PBRs as erosional features carved into the bedrock via wind abrasion, whose spacing is determined by the scale of flow separations. Montgomery et al. (2012) interpreted the ridges to have formed transverse to the prevailing wind-direction (Figure 18c) based on the orientation of PBR crests relative to yardangs and nearby active aeolian bedforms. Hugenholtz et al. (2015) defined PBRs as "aeolian-derived ridges carved into bedrock," but favored a model based on an Earth analog in Argentina in which preferential erosion in the spaces between migrating gravel megaripples results in transverse bedrock ridges

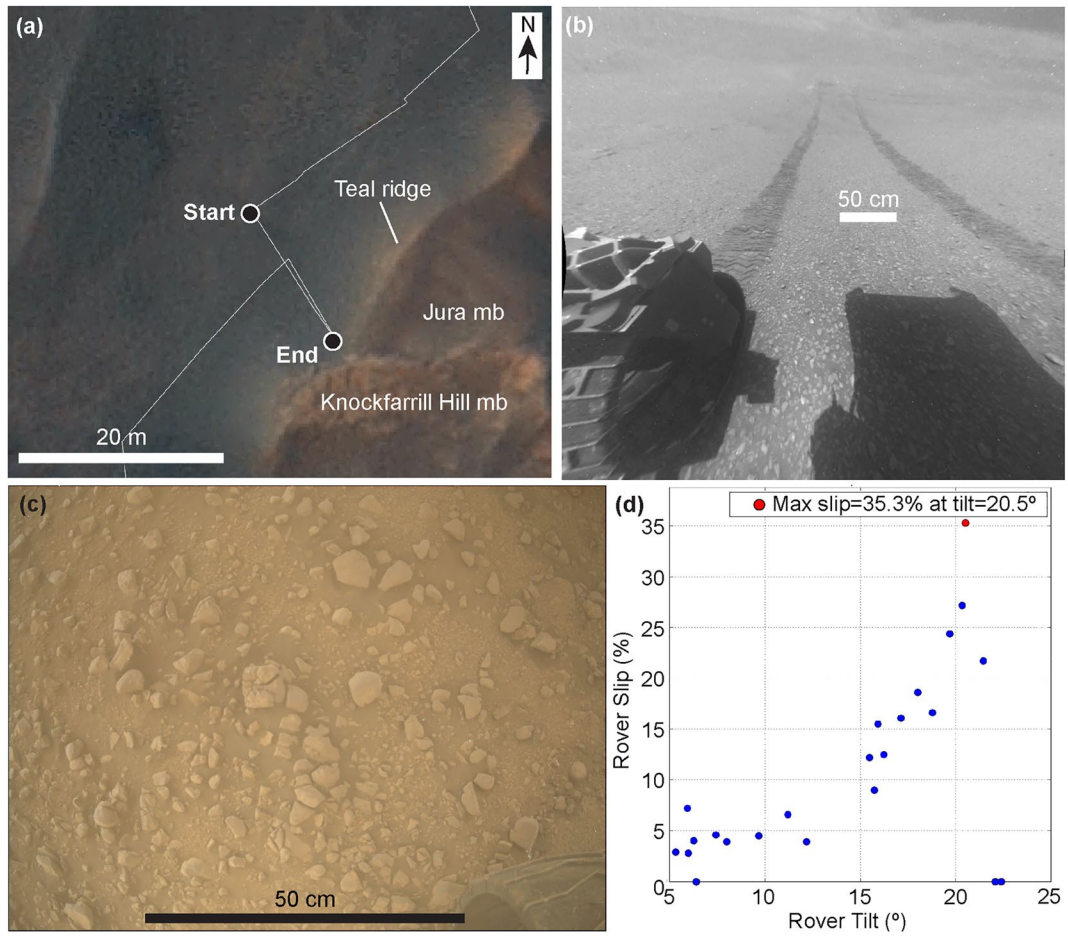

Figure 17. Mobility data from the Sol 2439 drive up a ridge flank. (a) High Resolution Imaging Science Experiment (HiRISE) map showing the start and end of the sol 2439 drive. The center coordinate (lat, lon) of the area shown is −4.7282, 137.3840. HiRISE image ID: ESP_039280_1755. North is up for (a); illumination from the left. (b) Left rear Hazcam image (RLB_614017643RAS_T0760988RHAZ00311M1) acquired on sol 2439 showing wheel tracks up the flank of the ridge. (c) MARDI image (2439MD0009590000201707E01) acquired at the end of the drive on sol 2439 showing clasts on the flank of the ridge. (d) Plot of rover slip versus tilt during the 2439 drive.

protected from erosion by the megaripples (Figure 18d). Silvestro et al. (2021) and Favaro et al. (2021) favored a model similar to that proposed by Hugenholtz et al. (2015) to explain PBRs in Oxia Planum, Mars.

Given that there is not yet consensus on the process by which PBRs form, and given the relative nascency of PBR studies, we use the term "PBR" as originally defined by Montgomery et al. (2012) and Hugenholtz et al. (2015) to refer to ridges with megaripple-like morphology carved from bedrock by the wind. This definition implies formation by wind erosion, but is otherwise non-genetic since it does not invoke a specific process of wind, bedrock, or bedform interaction, nor a formative wind direction. The following evidence from orbiter data supports an interpretation and designation of the Glen Torridon ridges as erosional PBRs: the ridges exhibit linear to slightly sinuous morphology and sometimes exhibit bifurcations, ridges lack a streamlined, teardrop shape or inverted ship's hull asymmetry, are decameter-scale in length, and exhibit decameter-scale regular spacing, and the ridges crosscut member boundaries and are discordant with expected bedding orientation, spanning several meters in elevation from end-to-end. The ridges are also disrupted by small impact craters, further supporting the coherency, induration, and prolonged exposure of the ridges at the surface.

Curiosity rover data supports an interpretation and designation of these ridges as PBRs given the presence of bedrock within and on the ridges, lack of internal aeolian cross-bedding, and the textural and compositional similarities between pebbles, cobbles, and in-place bedrock found on the flanks and crests of the ridges with inter-ridge bedrock, suggesting a very local source for the eroding pebbles and cobbles. The presence of exposed

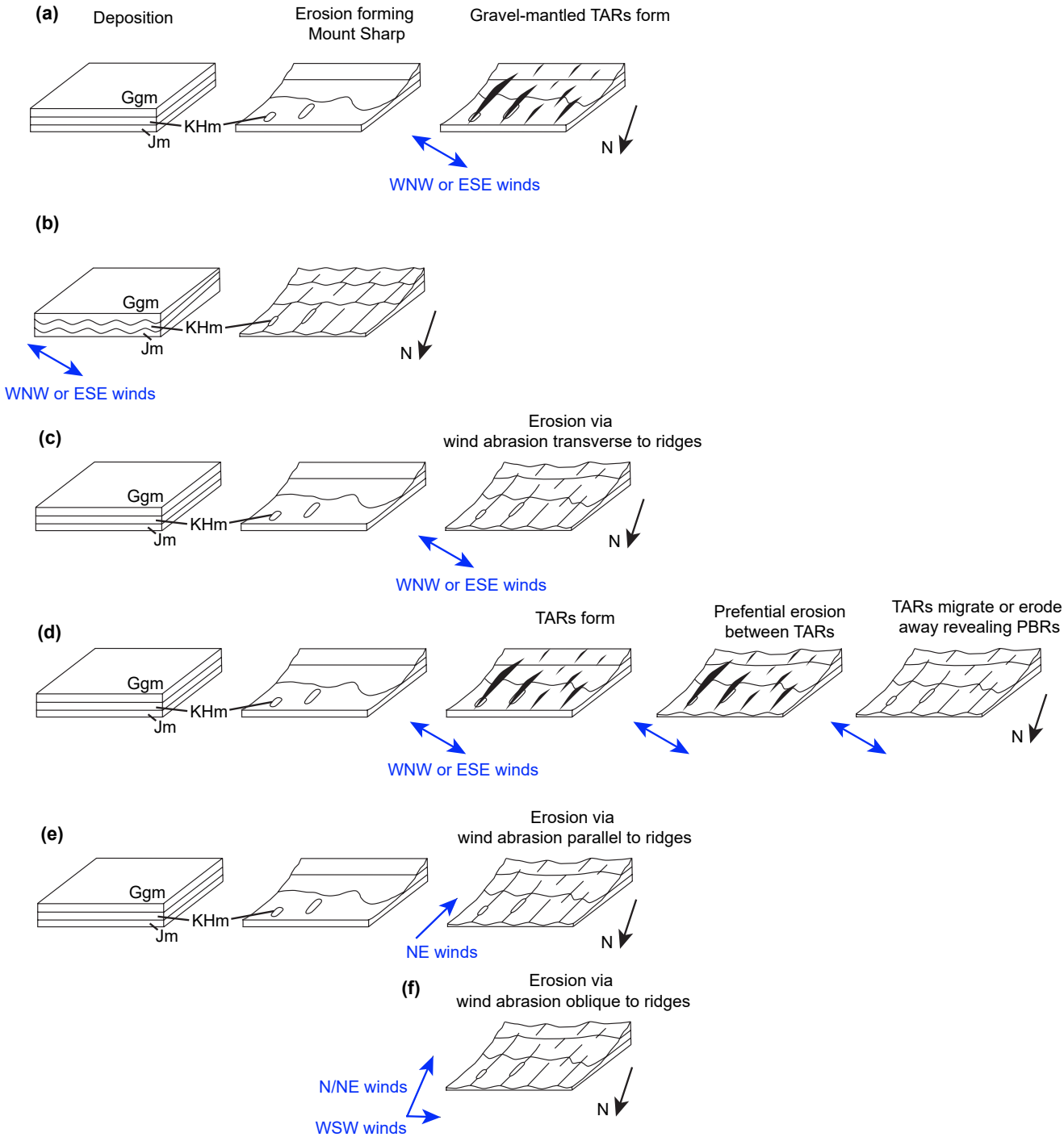

Figure 18. Possible scenarios for the formation of the Glen Torridon ridges. Blue arrows indicate dominant or net wind regimes implied by the scenario. (a) Gravel-mantled unconsolidated constructional bedforms present today, (b) exhumation of paleobedforms within the Jura, Knockfarril Hill, and Glasgow members, (c) erosional ridges carved into the Glen Torridon bedrock after the exhumation of Mount Sharp by winds transverse to the ridges, (d) erosional ridges forming in exposed bedrock between armoring bedforms (either unconsolidated or indurated) unconformably overlying the Jura, Knockfarril Hill, and Glasgow members after the exhumation of Mount Sharp, or (e) erosional ridges carved into the Glen Torridon bedrock after the exhumation of Mount Sharp by winds parallel or (f) oblique to the ridges.

bedrock along the flanks or at the crests of some ridges suggests that the pebbly regolith is relatively thin, likely no more than a few to ~10 cm thick. This is also consistent with, though not necessarily uniquely supported by, the observation of minimal sinkage of the rover's wheels into the crest and flanks of the ridges. The near ubiquitous regolith cover throughout northern Glen Torridon suggests prolonged exposure and physical weathering

Table 4
Summary of Wind Indicators in the Glen Torridon Region Relative to Periodic Bedrock Ridges (PBRs)

Relative age	Wind indicator	Orientation	Inferred wind direction	Orientation of GT PBRs relative to inferred wind direction
Modern	Eroded drill fines (Sullivan, Baker, et al., 2020)	W	W	Transverse
	MarsWRF Model Most Common Winds	SW, WSW, SSW	SW, WSW, SSW	Parallel
	Mars WRF Model Strongest Wind Stresses	SSW	SSW	Parallel
	Sand wind tails behind rocks and pebbles (Sullivan, Baker, et al., 2020)	WSW	WSW	Oblique
	Glen Torridon Active Ripple Crests (Sullivan, Baker, et al., 2020; this study)	N/S to NNE/SSW	W to WSW	Transverse to oblique
	Sands of Forvie Wind Streak (Sullivan, Baker, et al., 2020)	WSW	WSW	Transverse to oblique
Older	Glen Torridon TAR crests (this study)	NW/SE	NE or SW	Parallel
	Abrasion textures in Glasgow member (Sullivan, Baker, et al., 2020)	WNW to S	WNW to S	Transverse to parallel
	Abrasion textures in Stimson member (Sullivan, Baker, et al., 2020)	NE	NE	Parallel
Oldest	Greenheugh Pediment linear ridges (Anderson & Bell, 2010; Kronyak et al., 2019)	WNW/ESE	Unknown	Unknown
	Scours and canyons near Glen Torridon (this study)	SE to SW	SE to SW	Oblique to parallel
	Yardangs on the NW face of Mount Sharp (this study)	NNE/SSW	SSW	Oblique to parallel

at the surface of the bedrock ridges and surrounding terrain, including via aeolian processes. The following questions then remain: what was the orientation of the Glen Torridon PBRS relative to the formative wind direction(s) and how were these ridges carved into the bedrock?

5.2. Examining Evidence for PBR Formative Wind Directions

5.2.1. PBR Formation by Transverse Winds

Previous studies have suggested that PBR orientation is a directional indicator of the dominant, prevailing formational wind regime. To support the interpretation that PBRs form transverse to the wind (i.e., Figure 18c), Montgomery et al. (2012) compared the orientation of PBRs at several sites on Mars to: (a) nearby active aeolian bedforms like ripples and dunes, and (b) longer time-scale erosional bedrock features like yardangs. Montgomery et al. (2012) observed that PBRs were typically aligned with transverse wind indicators like active ripples and dunes, and oriented orthogonal to yardangs elongated parallel to the dominant wind direction. The process of transverse PBR formation proposed by Hugenholtz et al. (2015) predicts that PBRs and nearby megaripples/TARs, if they are still present, should be aligned in their crest orientations (Figure 18d). Favaro et al. (2021) and Silvestro et al. (2021) interpret the orientation of younger TARs relative to older PBRs at Oxia Planum as evidence for a change in paleowinds compared to more modern regimes.

If the Glen Torridon PBRs formed transverse to the dominant or net formational wind regime via the models proposed by Montgomery et al. (2012) and Hugenholtz et al. (2015), we would infer formational winds oriented orthogonally (WNW/ESE, ~288°/108°) to the PBRs. The orientation of the Glen Torridon PBRs relative to other local wind indicators ranging from modern to older inactive bedforms to oldest bedrock erosional features is shown in Table 4. Some modern wind indicators including eroding Curiosity drill fines, sand wind tails behind rocks and pebbles, N-S oriented active dark ripples, and the Sands of Forvie wind streak suggest present-day sand transport to the W within Glen Torridon (Sullivan, Baker, et al., 2020) that would be approximately orthogonal to the PBRs oriented more directly N-S. However, most modern wind indicators suggest winds blowing to the WSW (Sullivan, Baker, et al., 2020) and most PBRs are oriented to the NE.

The inactive bright TARs throughout Glen Torridon have a tight crest distribution oriented NW-SE, ~90° offset from the orientation that transverse formative winds would predict. There are relatively few streamlined hills or yardangs in the immediate vicinity of Glen Torridon, but those present upslope along the NW face of Mount

Sharp (Figure 10c) show fairly consistent orientations NNW-SSE to NNE-SSW, significantly offset from the orientation expected for transverse PBR paleowinds.

Although Montgomery et al. (2012) used modern, active aeolian bedform orientations to support the transverse PBR interpretation, and Hugenholtz et al.'s (2015) model implies a potential relationship between ridges and nearby megaripples/TARs, it is not surprising that modern aeolian landforms in Glen Torridon would not align as expected with transverse PBR-forming winds given that the PBRs are likely significantly older than active ripples, sand shadows, or local wind streaks and could have formed under a different paelowind regime. It is striking that the Glen Torridon TARs appear nearly perfectly orthogonal to the PBRs (Figure 9), but changing paleowind directions through time could explain this offset as well, as was invoked by Favaro et al. (2021) and Silvestro et al. (2021) to explain a similar local offset between co-occurring TARs and PBRs in Oxia Planum. If the Glen Torridon PBRs are indicators of a formational paleowind regime transverse to the ridge crests, this wind regime would be distinct from both the modern local wind regime, that responsible for older TARs, as well as the integrated, long-term, prevailing northerly wind regime that formed the streamlined bedrock hills, yardangs, and scours on the NW face of Mount Sharp.

The Hugenholtz et al. (2015) model for transverse PBRs on Mars invokes preferential erosion of bedrock in the spaces between unconsolidated TARs. Close spatial associations, including mantling, between PBRs and TARs at a number of sites on Mars (Sneed et al., 2020) offers support for this formation scenario, as do Earth analogs for PBRs in Argentina (Hugenholtz et al., 2015). In Glen Torridon, we do not observe the inactive bright TARs to be aligned with the orientation of the Glen Torridon ridges (Figure 9) suggesting that if an armoring model explains PBR formation in Glen Torridon, the TAR field responsible for ridge formation detached from the Glen Torridon ridges and dissipated or eroded completely. This would have had to occur prior to the creation and persistence of both the modern dark rippled sand patches and the TAR-like bedforms oriented orthogonal to the ridges today. An advantage of the Hugenholtz et al. (2015) model for PBR formation is its ability to explain ridge bifurcations as the relatively straightforward reflection in the bedrock of well-understood granular bedform interactions (i.e., Landry & Werner, 1994; Kocurek & Ewin, 2005). The Hugenholtz et al. (2015) model can also explain the regular spacing of PBRs as inherited periodicity from the bedforms that overlain the bedrock, whereas the Montgomery et al. (2012) model relies on a theoretical relationship between ridge spacing and flow separation that has not yet been verified in the lab or field at the scale of PBR landforms on Earth and Mars. While appealing, the Hugenholtz et al. (2015) model of PBR formation is difficult to test at Glen Torridon given the lack of evidence to support the past existence of such an extensive field of aligned TARs in the region.

5.2.2. PBR Formation by Parallel or Oblique Winds

Although previous PBR studies have all favored a flow transverse model for PBR formation (Favaro et al., 2021; Hugenholtz et al., 2015; Montgomery et al., 2012; Silvestro et al., 2021), the modern-day wind stress results from MarsWRF simulations, near perfect orthogonal relationship between the Glen Torridon PBRs and TARs, and the known regional context of long time-scale northerly winds (Day & Kocurek, 2016) suggest that flow-parallel or flow-oblique models of Glen Torridon PBR formation are worth considering (Figures 18e and 18f). Sand-driving winds blowing NE are also recorded by abrasion textures located just outside the Glen Torridon trough, on Stimson sandstone outcrops on the Naukluft plateau and the Greenheugh pediment, locations which could better preserve relatively old indications of past wind conditions due to relative isolation from currently active sands (Banham, Gupta, Bryk, et al., 2021; Banham, Gupta, Rubin, et al., 2021; Banham et al., 2018; Sullivan, Baker, et al., 2020; Schieber et al., 2020).

The Glen Torridon PBRs align well with the orientation of present-day MarsWRF model results and local TARs in a parallel formative wind model, but they are still rotated by up to a few tens of degrees from the commonly observed NNW-SSE orientation of older, longer time-scale yardangs and streamlined hills further up Mount Sharp (Figure 10c). We propose that the specific topography of the Glen Torridon trough, with Vera Rubin ridge to the north, and the Greenheugh pediment and slope of Mount Sharp to the south, could have resulted in the local diversion of northerly winds flowing up and over VRR toward the SW, possibly creating a NE to SW wind regime local to Glen Torridon that carved ridges parallel to the dominant wind direction, rather than transverse as typically assumed for PBRs. Alternatively, the integrated effect of multi-directional

winds including shorter-time scale winds to the WSW local to the Glen Torridon trough combined with longer-term northerly regional winds (i.e., Day & Kocurek, 2016) could have resulted in a net NE to SW wind regime specific to Glen Torridon capable of carving the PBRs oblique to the dominant winds that contributed to their formation.

Previous studies have made the case against a flow-parallel origin for PBRs given that the ridges do not exhibit the typical asymmetrical morphology with a blunt, steep upwind end that tapers and lowers downwind considered characteristic of flow-parallel yardangs (Montgomery et al., 2012; Silvestro et al., 2021). Although the GT ridges do not conform with classic yardang characteristics, flow-parallel wind-eroded bedrock ridges exhibit diverse morphologies (Kerber, 2016), and a large number of factors can influence their shape. These factors include the extent of deflation versus abrasion (Kerber, 2016), substrate strength and heterogeneity including structure and layering (de Silva et al., 2010; Hu et al., 2017; Pelletier et al., 2018), preexisting topography (Perkins et al., 2015), wind direction (e.g., Wang et al., 2018), and on Earth the role of water erosion (Dong et al., 2012; Laity, 2011; Pelletier et al., 2018).

A complete mechanistic model for PBR formation by parallel or oblique winds is beyond the scope of the present study, but given: (a) the supporting orientation of aeolian features in and around Glen Torridon coupled with, (b) a complex setting involving a sloping surface in a unique local topographic setting, (c) the potential influence of multiple wind regimes acting over varying timescales, and (d) internal stratigraphy with varying lithology, this study of the Glen Torridon PBRs and other modern and ancient wind indicators in the region suggest that flow-transverse paleowind regimes should be considered but not assumed, and that the feasibility of a flow-parallel or oblique origin for PBRs is worthy of future study.

5.3. Depositional and Environmental Implications of the Glen Torridon PBRs

The interpretation of the Glen Torridon ridges as erosional bedrock ridges has important implications for the depositional origin of the Murray and lower Carolyn Shoemaker formations exposed within the Glen Torridon region. Milliken et al. (2014) proposed that the Glen Torridon ridges were aeolian paleobedforms, and thus provided evidence for an aeolian depositional interpretation for the rocks of the Glen Torridon area. Given that evidence strongly supports an erosional, rather than constructional origin for the ridges, this study concludes no connection between the formation of the ridges and the primary depositional process by or environment in which the Glen Torridon rocks formed. This study's interpretation of the ridges as post-depositional erosional features formed after the deposition of the units of the Gale mound is consistent with the ground-based lacustrine and fluvial interpretation for the rocks of Jura, Knockfarril Hill, Glasgow members (Carvaaca et al., 2021; Edgar et al., 2020; Fedo et al., 2019).

This study examines the evidence for transverse, parallel, oblique PBR formative wind regimes. Although the morphology of the Glen Torridon PBRs is most easily explained by a transverse formative wind regime, the orientation of the nearby active aeolian features supporting the presence of local E to W sand-driving winds (Sullivan, Baker, et al., 2020) integrated with long timescale northerly regional winds (Day & Kocurek, 2016) in the unique topographic setting of the Glen Torridon trough makes a flow parallel or oblique origin for the Glen Torridon PBRs attractive. The misalignment of PBR long axes compared with current primary and secondary wind directions suggests that the Glen Torridon ridges formed over longer time periods exceeding the current seasonally varying combination of regional and slope-controlled wind directions that influence active dark sand ripples, sandy wind tails, and the erosion of MSL drill tailings piles. Whether formed transverse, parallel, or oblique to formative winds, the Glen Torridon ridges likely formed under past sand-driving wind conditions somewhat different from today.

Abundant yardangs, TARs, ventifacts, and even paleobedforms have been observed elsewhere in Gale crater, but a well-defined series of PBRs has only been observed by Curiosity in the Glen Torridon area. Soft, clay-bearing rocks were observed earlier in Curiosity's exploration of the Murray formation, but the rocks observed in Glen Torridon are the most clay-rich yet observed by the rover (Bristow et al., 2021), and in family with, if not the softest rocks, drilled by Curiosity. PBRs are not observed on the harder, more resistant Vera Rubin ridge, and PBRs decrease in frequency up-section from the very weak GT Jura to the slightly harder, more cohesive sand-

stones and mixed sandstones and mudstones of the Knockfarril Hill and Glasgow members, respectively. The local topography of the Glen Torridon region may also contribute to the conditions conducive to PBR formation in this region of Mount Sharp, although the orientation of ridges appear largely agnostic to the presence of VRR or the Greenheugh pediment. The presence of Vera Rubin ridge could affect regional winds by compressing the flow up and over VRR, resulting in increased flow speeds and greater erosive capabilities by aeolian abrasion in the slight topographic depression behind VRR in the Glen Torridon trough. As the wind continues climbing out of the Glen Torridon depression and away from the VRR, flow speeds would decrease, which, when coupled with harder rocks south of Glen Torridon, could prohibit the formation of the ridges to the south and upslope on Mount Sharp.

6. Conclusions

1. The series of regularly spaced, curvilinear ridges oriented NE-SW spanning over 8 km in the Glen Torridon region of Mount Sharp are interpreted as erosional PBRs formed after the exhumation of Mount Sharp.
2. Glen Torridon PBRs are typically decameters long, one to several meters in height, and spaced between 10 and 30 m apart. Some PBRs are symmetrical with well-defined crests and troughs, while many others are asymmetrical. Where ridge orientation aligns with the expected strike of bedding, ridges sometimes have a bench-like morphology.
3. PBRs in the Glen Torridon Jura are typically covered at the surface by a layer of sand, pebbles, and cobbles, but rover mobility data and image observations are consistent with this layer being thin with an indurated bedrock substrate beneath. PBRs in the Knockfarril Hill and Glasgow members are more obviously comprised of indurated bedrock.
4. The morphology of the Glen Torridon PBRs, including their shape and the presence of bifurcations, is consistent with a transverse formative wind regime. If formed by transverse winds, the GT PBRs record a dominant or net wind regime distinct from those represented by other modern short time-scale and ancient, long time-scale wind indicators on the NW slope of Mount Sharp.
5. The orientation of the Glen Torridon PBRs relative to MarsWRF model outputs of predicted wind stress, nearby TARs, scours, and streamlined mounds and ridges further up the slope of Mount Sharp may support an interpretation of the PBRs as flow-parallel or flow-oblique features. Future work should consider flow transverse, parallel, and oblique wind regimes for PBR formation.
6. Given the favored interpretation for the PBRs in the Glen Torridon area as post-depositional erosional features, they should not be used to interpret the primary depositional origin of the Mount Sharp strata in which they occur.

Data Availability Statement

All Mars Science Laboratory Curiosity data products and data sets, including Mars Descent Imager (Malin, 2013a), Mastcam (Malin, 2013b), Rear Hazcam (Maki, 2013a), and Navcam (Maki, 2013b) images and Alpha Particle X-ray Spectrometer (Gellert, 2013) data are archived at the NASA Planetary Data Systems and are available at https://pds-geosciences.wustl.edu/missions/msl/. The High Resolution Imaging Science Experiment (HiRISE) digital elevation model (Calef & Parker, 2016b) is available at https://astrogeology.usgs.gov/search/map/Mars/MarsScienceLaboratory/Mosaics/MSL_Gale_DEM_Mosaic_10m. The HiRISE grayscale merged orthophoto (Calef & Parker, 2016a) on which the color mosaic is based, is available at https://astrogeology.usgs.gov/search/map/Mars/MarsScienceLaboratory/Mosaics/MSL_Gale_Orthophoto_Mosaic_10m_v3. Individual HiRISE images, including color images, are available at https://www.uahirise.org/ and are archived at the NASA Planetary Data Systems at https://pds-imaging.jpl.nasa.gov/volumes/mro.html. Compact Reconnaissance Imaging Spectrometer for Mars (CRISM) data (Murchie, 2006) is archived at the NASA Planetary Data Systems and are available at https://pds-geosciences.wustl.edu/missions/mro/crism.htm. All other data products related to the CRISM-derived thermal inertia values presented in this paper can be accessed through Christian et al. (2021; Digital Research Materials) and are available at https://doi.org/10.7936/jznj-s510. Glen Torridon ridge, transverse aeolian ridge, and ripple shapefiles, as well as shapefiles showing the locations of wavelength profiles and individual ridge topographic profiles are available from Stack (2021) at https://doi.org/10.5281/zenodo.6324330.

The Mars Weather Research and Forecasting modeling outputs used in this paper are available at Newman (2022) at https://doi.org/10.5281/zenodo.6514934.

Acknowledgments
This effort was carried out in part at the Jet Propulsion Laboratory, California Institute of Technology, and at the home institutions of the named co-authors under a contract with the National Aeronautics and Space Administration. The authors would like to acknowledge the scientists and engineers of the MSL Curiosity and MRO missions for acquiring and providing the data used in this study. Mastcam mosaics were processed by the Mastcam team at Malin Space Science Systems. Fred Calef provided context on the orbiter basemaps used in this study and provided guidance regarding impact craters and crater retention ages. Laura Kerber shared her expertise on yardangs and other aeolian erosion features.
The authors would like to thank and acknowledge Dr. Elena Favaro and two anonymous reviewers of this manuscript whose comments substantially improved this paper. Any use of trade, firm, or product names is for descriptive purposes only and does not imply endorsement by the U.S. government.

References

Anderson, R., Edgar, L. A., Rubin, D. M., Lewis, K. W., & Newman, C. (2018). Complex bedding geometry in the upper portion of Aeolis Mons, Gale crater, Mars. *Icarus*, *314*, 246–264. https://doi.org/10.1016/j.icarus.2018.06.009

Anderson, R. B., & Bell, J. F., III (2010). Geologic mapping and characterization of Gale Crater and implications for its potential as a Mars Science Laboratory landing site. *MARS*, *5*, 76–128. https://doi.org/10.1555/mars.2010.0004

Arvidson, R. E. (1974). Wind-blown streaks, splotches, and associated craters on Mars: Statistical analysis of Mariner 9 photographs. *Icarus*, *21*(1), 12–27. https://doi.org/10.1016/0019-1035(74)90086-4

Arvidson, R. E., Iagnemma, K. D., Maimone, M., Fraeman, A. A., Zhou, F., Heverly, M. C., et al. (2017). Mars Science Laboratory curiosity rover megaripple crossings up to sol 170 in Gale Crater. *Journal of Field Robotics*, *34*(3), 495–518. https://doi.org/10.1002/rob.21647

Baker, M. M., Lapotre, M. G. A., Minitti, M. E., Newman, C. E., Sullivan, R., Weitz, C. M., et al. (2018). The Bagnold Dunes in southern summer: Active sediment transport on Mars observed by the Curiosity rover. *Geophysical Research Letters*, *45*(17), 8853–8863. https://doi.org/10.1029/2018GL079040

Baker, M. M., Newman, C. E., Lapotre, M. G. A., Sullivan, R., Bridges, N. T., & Lewis, K. W. (2018). Coarse sediment transport in the modern Martian environment. *Journal of Geophysical Research: Planets*, *123*(6), 1380–1394. https://doi.org/10.1002/2017JE005513

Baker, M. M., Newman, C. E., Sullivan, R., Minitti, M. E., Edgett, K. S., Fey, D., et al. (2022). Diurnal variability in aeolian sediment transport at Gale crater, Mars. *Journal of Geophysical Research*, *127*(2), e2020JE006734. https://doi.org/10.1029/2020JE006734

Balme, M., Berman, D. C., Bourke, M. C., & Zimbelman, J. R. (2008). Transverse aeolian ridges (TARs) on Mars. *Geomorphology*, *101*(4), 703–720. https://doi.org/10.1016/j.geomorph.2008.03.011

Banham, S. G., Gupta, S., Bryk, A. B., Rubin, D. M., Edgett, K. S., Dietrich, W. E., et al. (2021). Reconstruction of aeolian palaeoenvironments and past climate events at the Greenheugh pediment, Aeolis Mons, Mars. *Presented at the 52nd Lunar and Planetary Science Conference, Virtual Meeting*.

Banham, S. G., Gupta, S., Rubin, D. M., Edgett, K. S., Barnes, R., Van Beek, J., et al. (2021). A rock record of complex aeolian bedforms in a Hesperian desert landscape: The Stimson formation as exposed in the Murray buttes, Gale Crater, Mars. *Journal of Geophysical Research: Planets*, *126*(4). https://doi.org/10.1029/2020JE006554

Banham, S. G., Gupta, S., Rubin, D. M., Watkins, J. A., Sumner, D. Y., Edgett, K. S., et al. (2018). Ancient Martian aeolian processes and palaeomorphology reconstructed from the Stimson formation on the lower slope of Aeolis Mons, Gale Crater, Mars. *Sedimentology*, *65*(4), 993–1042. https://doi.org/10.1111/sed.12469

Bell, J. F., III, Godber, A., McNair, S., Caplinger, M. A., Maki, J. N., Lemmon, M. T., et al. (2017). The Mars Science Laboratory Curiosity rover Mastcam instruments: Preflight and in-flight calibration, validation, and data archiving. *Earth and Space Science*, *4*(7), 396–452. https://doi.org/10.1002/2016ea000219

Bennett, K., Fox, V. K., Bryk, A., Fedo, C., Vasavada, A. R., Dehouck, E., et al. (2019). Results from the Curiosity rover's traverse through the clay-bearing Glen Torridon region in Gale Crater. *Presented at the AGU Fall Meeting 2019*.

Berman, D. C., Balme, M. R., Michalski, J. R., Clark, S. C., & Joseph, E. C. S. (2018). High-resolution investigations of transverse aeolian ridges on Mars. *Icarus*, *312*, 247–266. https://doi.org/10.1016/j.icarus.2018.05.003

Berman, D. C., Balme, M. R., Rafkin, S. C. R., & Zimbelman, J. R. (2011). Transverse aeolian ridges (TARs) on Mars II: Distributions, orientations, and ages. *Icarus*, *213*(1), 116–130. https://doi.org/10.1016/j.icarus.2011.02.014

Bibring, J.-P., Langevin, Y., Mustard, J. F., Poulet, F., Arvidson, R., Gendrin, A., et al. (2006). Global mineralogical and aqueous Mars history derived from OMEGA/Mars express data. *Science*, *312*(5772), 400–404. https://doi.org/10.1126/science.1122659

Blake, D., Vaniman, D., Achilles, C., Anderson, R., Bish, D., Bristow, T., et al. (2012). Characterization and calibration of the CheMin mineralogical instrument on Mars Science Laboratory. *Space Science Reviews*, *170*(1–4), 341–399. https://doi.org/10.1007/s11214-012-9905-1

Bridges, N., & Ehlmann, B. L. (2018). The Mars Science Laboratory (MSL) Bagnold dunes campaign, phase I: Overview and introduction to the special issue. *Journal of Geophysical Research: Planets*, *123*(1), 3–19. https://doi.org/10.1002/2017JE005401

Bridges, N., Geissler, P., Silvestro, S., & Banks, M. (2013). Bedform migration on Mars: Current results and future plans. *Aeolian Research*, *9*, 133–151. https://doi.org/10.1016/j.aeolia.2013.02.004

Bridges, N. T., Calef, F. J., Hallet, B., Herkenhoff, K. E., Lanza, N. L., LeMouélic, S., et al. (2014). The rock abrasion record at Gale Crater: Mars Science Laboratory results from Bradbury landing to rocknest. *Journal of Geophysical Research: Planets*, *119*(6), 1374–1389. https://doi.org/10.1002/2013JE004579

Bridges, N. T., Geissler, P. E., McEwen, A. S., Thomson, B. J., Chuang, F. C., Herkenhoff, K. E., et al. (2007). Windy Mars: A dynamic planet as seen by the HiRISE camera. *Geophysical Research Letters*, *34*, L23205. https://doi.org/10.1029/2007GL031445

Bridges, N. T., Sullivan, R., Newman, C. E., Navarro, S., van Beek, J., Ewing, R. C., et al. (2017). Martian aeolian activity at the Bagnold Dunes, Gale Crater: The view from the surface and orbit. *Journal of Geophysical Research: Planets*, *122*(10), 2077–2110. https://doi.org/10.1002/2017JE005263

Bristow, T. F., Grotzinger, J. P., Rampe, E. B., Cuadros, J., Chipera, S. J., Downs, G. W., et al. (2021). Brine-driven destruction of clay minerals in Gale Crater, Mars. *Science*, *373*(6551), 198–204. https://doi.org/10.1126/science.abg5449

Bristow, T. F., Rampe, E. B., Grotzinger, J. P., Fox, V. K., Bennett, K. A., Yen, A. S., et al. (2019). Clay minerals of Glen Torridon, Mount Sharp, Gale Crater, Mars. *Paper presented at the Ninth International Conference on Mars*.

Calef, F. J., III, Dietrich, W. E., Edgar, L., Farmer, J., Fraeman, A., Grotzinger, J., et al. (2013). Geologic mapping of the Mars Science Laboratory landing ellipse. *Paper presented at the 44th Lunar and Planetary Science Conference*.

Calef, F. J., III, & Parker, T. (2016a). *MSL Gale merged DEM 1m v3*. PDS Annex. U.S. Geological Survey. Retrieved from http://bit.ly/MSL_Basemap

Calef, F. J., III, & Parker, T. (2016b). *MSL Gale merged orthophoto mosaic*. PDS Annex. U.S. Geological Survey. Retrieved from http://bit.ly/MSL_Basemap

Carvaaca, G., Mangold, N., Dehouck, E., Schieber, J., Bryk, A. B., Fedo, C. M., et al. (2021). Evidence of depositional settings variation at the Jura/Knockfarril hill members transition in the glen Torridon region (Gale Crater, Mars). *Paper presented at the 52nd Lunar and Planetary Science Conference, Virtual Meeting*.

Chojnacki, M., Fenton, L. K., Weintraub, A. R., Edgar, L. A., Jodhpurkar, M. J., & Edwards, C. S. (2020). Ancient Martian aeolian sand dune deposits recorded in the stratigraphy of Valles Marineris and implications for past climates. *Journal of Geophysical Research: Planets*, *125*(9). https://doi.org/10.1029/2020JE006510

Christian, J. R., Arvidson, R. E., O'Sullivan, J. A., Vasavada, A. R., & Weitz, C. M. (2021). CRISM-based high spatial resolution thermal inertia mapping along Curiosity's traverses in Gale Crater. *Digital Research Materials (Data & Supplemental Files)*, 88. https://doi.org/10.7936/jznj-s510

Christian, J. R., Arvidson, R. E., O'Sullivan, J. A., Vasavada, A. R., & Weitz, C. M. (2022). CRISM-based high spatial resolution thermal inertia mapping along Curiosity's traverses in Gale Crater. *Journal of Geophysical Research: Planets*. https://doi.org/10.1029/2021JE007076

Cousin, A., Desjardin, M., Dehouck, E., Forni, O., David, G., Berger, G., et al. (2021). K-rich rubbly bedrock at Glen Torridon, Gale Crater, Mars: Investigating the possible presence of illite. *Paper presented at the 52nd Lunar and Planetary Science Conference, Virtual Meeting*.

Cutts, J. A., & Smith, R. S. U. (1973). Eolian deposits and dunes on Mars. *Journal of Geophysical Research*, *78*(20), 4139–4154. https://doi.org/10.1029/JB078i020p04139

Day, M., & Kocurek, G. (2016). Observations of an aeolian landscape: From surface to orbit in Gale Crater. *Icarus*, *280*, 37–71. https://doi.org/10.1016/j.icarus.2015.09.042

Dehouck, E., Cousin, A., Mangold, N., Frydenvang, J., Gasnault, O., Forni, O., et al. (2022). Bedrock geochemistry and alteration history of the clay-bearing Glen Torridon region of Gale Crater, Mars. *Journal of Geophysical Research: Planets*, *127*, e2021JE007103. https://doi.org/10.1029/2021JE007103

de Silva, S. L., Bailey, J. E., Mandt, K. E., & Virmonte, J. M. (2010). Yardangs in terrestrial ignnimbrites: Synergistic remote and field observations on Earth with applications to Mars. *Planetary and Space Science*, *58*(4), 459–471. https://doi.org/10.1016/j.pss.2009.10.1002

Dong, Z., Lv, P., Lu, J., Qian, G., Zhang, Z., & Luo, W. (2012). Geomorphology and origin of Yardangs in the Kumtagh Desert, Northwest China. *Geomorphology*, *139–140*, 145–154. https://doi.org/10.1016/j.geomorph.2011.10.012

Dromart, G., Le Deit, L., Rapin, W., Gasnault, O., Le Mouélic, S., Quantin-Nataf, C., et al. (2021). Deposition and erosion of light-toned Yardang-forming unit of Mt Sharp, Gale Crater, Mars. *Earth and Planetary Science Letters*, *554*, 116681. https://doi.org/10.1016/j.epsl.2020.116681

Edgar, L. A., Fedo, C. M., Gupta, S., Banham, S. G., Fraeman, A. A., Grotzinger, J. P., et al. (2020). A lacustrine paleoenvironment recorded at Vera Rubin Ridge, Gale Crater: Overview of the sedimentology and stratigraphy observed by the Mars Science Laboratory Curiosity Rover. *Journal of Geophysical Research- Planets*, *125*(3). https://doi.org/10.1029/2019JE006307

Edgar, L. A., Gupta, S., Rubin, D. M., Lewis, K. W., Kocurek, G. A., Anderson, R. B., et al. (2017). Shaler: In situ analysis of a fluvial sedimentary deposit on Mars. *Sedimentology*, *65*(1), 96–122. https://doi.org/10.1111/sed.12370

Edgett, K. S., & Malin, M. C. (2000). New view of Mars eolian activity, materials, and surface properties: Three vignettes from the Mars Global Surveyor Mars Orbiter Camera. *Journal of Geophysical Research*, *105*(E1), 1623–1650. https://doi.org/10.1029/1999JE001152

Ewing, R. C., Aymeric-Pierre, B. P., Kocurek, G., & Bourke, M. (2010). Dune field pattern formation and recent transporting winds in the Olympia Undae Dune Field, north polar region of Mars. *Journal of Geophysical Research*, *115*(E8), E08005. https://doi.org/10.1029/2009JE003526

Favaro, E. A., Balme, M. R., Davis, J. M., Grindrod, P. M., Fawdon, P., Barrett, A. M., & Lewis, S. R. (2021). The aeolian environment of the landing site for the ExoMars Rosalind Franklin Rover in Oxia Planum, Mars. *Journal of Geophysical Research: Planets*, *126*(4), 2020JE006723. https://doi.org/10.1029/2020JE006723

Fedo, C. M., Edgar, L. A., Bryk, A. B., Grotzinger, J. P., Gwizd, S. A., Banham, S., et al. (2021). Stratigraphic-based bedrock geologic map of the Murray and Carolyn Shoemaker formations along the traverse of the Curiosity rover. *Paper presented at The Geological Society of London William Smith Virtual Meeting 2021*.

Fedo, C. M., Grotzinger, J. P., Gupta, S., Banham, S., Bennett, K., Edgar, L., et al. (2019). Evidence for persistent, water-rich, lacustrine deposition preserved in the Murray formation, Gale Crater: A depositional system suitable for sustained habitability. *Paper presented at the Ninth International Conference on Mars*.

Fox, V. K., Bennett, K. A., Bryk, A. B., Fedo, C., Arvidson, R., Dehouck, E., et al. (2021). Contextualizing CRISM observations of the clay-bearing Glen Torridon region with the Mars Science Laboratory Curiosity Rover. *Paper presented at the 52nd Lunar and Planetary Science Conference, Virtual Meeting*.

Fraeman, A. A., Arvidson, R. E., Catalano, J. G., Grotzinger, J. P., Morris, R. V., Murchie, S. L., et al. (2013). A hematite-bearing layer in Gale Crater, Mars: Mapping and implications for past aqueous conditions. *Geology*, *41*(10), 1103–1106. https://doi.org/10.1130/G34613.1

Fraeman, A. A., Edgar, L. A., Rampe, E. B., Thompson, L. M., Frydenvang, J., Fedo, C. M., et al. (2020). Evidence for a diagenetic origin of Vera Rubin Ridge, Gale Crater, Mars: Summary and synthesis of Curiosity's exploration campaign. *Journal of Geophysical Research- Planets*, *125*(12). https://doi.org/10.1029/JE006527

Fraeman, A. A., Ehlmann, B. L., Arvidson, R. E., Edwards, C. S., Grotzinger, J. P., Milliken, R. E., et al. (2016). The stratigraphy and evolution of lower Mount Sharp from spectral, morphological, and thermophysical orbital data sets. *Journal of Geophysical Research-Planets*, *121*(9), 1713–1736. https://doi.org/10.1002/2016JE005095

Geissler, P. E. (2014). The birth and death of transverse aeolian ridges on Mars. *Journal of Geophysical Research: Planets*, *119*(12), 2583–2599. https://doi.org/10.1002/2014JE004633

Geissler, P. E., & Wilgus, J. T. (2017). The morphology of transverse aeolian ridges on Mars. *Aeolian Research*, *26*, 63–71. https://doi.org/10.1016/j.aeolia.2016.08.008

Gellert, R. (2013). *Mars Science Laboratory Alpha Particle X-ray Spectrometer RDR Data V1.0*. MSL-M-APXS-4/5-RDR-V1.0. NASA Planetary Data System.

Gellert, R., & Clark, B. C., III, & Mars Science Laboratory (MSL) Science Team. (2015). In situ compositional measurements of rocks and soils with the alpha particle X-ray spectrometer on NASA's Mars rovers. *Elements*, *11*(1), 39–44. https://doi.org/10.2113/gselements.11.1.39

Greeley, R., Kraft, M., Sullivan, R., Wilson, G., Bridges, N. T., Herkenhoff, K., et al. (1999). Aeolian features and processes at the Mars Pathfinder landing site. *Journal of Geophysical Research*, *104*(E4), 8573–8584. https://doi.org/10.1029/98JE02553

Greeley, R., Lee, S., & Thomas, P. (1992). Martian aeolian processes, sediments, and features. In H. H. Kieffer, B. M. Jakosky, C. W. Snyder, & M. S. Matthews (Eds.), *Mars* (pp. 730–766). The University of Arizona Press.

Grotzinger, J. P., Gupta, S., Malin, M. C., Rubin, D. M., Schieber, J., Siebach, K., et al. (2015). Deposition, exhumation, and paleoclimate of an ancient lake deposit, Gale Crater, Mars. *Science*, *350*(6257). https://doi.org/10.1126/science.aac7575

Grotzinger, J. P., Sumner, D. Y., Kah, L. C., Stack, K., Gupta, S., Edgar, L., et al. (2014). A Habitable Fluvio-lacustrine environment at Yellowknife Bay, Gale Crater, Mars. *Science*, *343*(6169). https://doi.org/10.1126/science.1242777

Gwizd, S., Fedo, C., Grotzinger, J., Edgett, K., Gupta, S., Stack, K. M., et al. (2019). Toward a greater understanding of cross-stratified facies in the Harmann's Valley Member of the Murray formation. *Paper presented at the Ninth International Conference on Mars*.

Hayward, R. K., Mullins, K. F., Fenton, L. K., Hare, T. M., Titus, T. N., Bourke, M. C., et al. (2007). Mars global digital dune database and initial science results. *Journal of Geophysical Research*, *112*, E11007. https://doi.org/10.1029/2007JE002943

He, L., Arvidson, R. E., O'Sullivan, J. A., Morris, R. V., Condus, T., Hughes, M. N., & Powell, K. E. (2022). Surface kinetic temperatures and nontronite single scattering albedo spectra from Mars Reconnaissance Orbiter CRISM hyperspectral imaging data over Glen Torridon, Gale Crater, Mars. *Journal of Geophysical Research: Planets*, *127*, e2021JE007092. https://doi.org/10.1029/2021JE007092

Hobbs, S. W., Paull, D. J., & Bourke, M. C. (2010). Aeolian processes and dune morphology in Gale Crater. *Icarus*, *210*(1), 102–115. https://doi.org/10.1016/j.icarus.2010.06.006

Hu, C., Chen, N., Kapp, P., Chen, J., Xiao, A., & Zhao, Y. (2017). Yardang geometries in the Qaidam Basin and their controlling factors. *Geomorphology*, *299*, 142–151. https://doi.org/10.1016/j.geomorph.2017.09.029

Hugenholtz, C. H., Barchyn, T. E., & Favaro, E. A. (2015). Formation of periodic bedrock ridges on Earth. *Journal of Aeolian Research*, *18*, 135–144. https://doi.org/10.1016/j.aeolia.2015.07.002

Hunt, A. R. G., Day, M., Edgett, K. S., & Chojnacki, M. (2022). The lithified aeolian dune field adjacent to the Apollinaris Sulci, Mars: Geological history and paleo-wind record. *Icarus*, *373*, 114788. https://doi.org/10.1016/j.icarus.2021.114788

Kerber, L. (2016). Controls on the morphology of Yardangs on the Earth and Mars. *Presented at the 47th Lunar and Planetary Science Conference, Abs. 2708*.

Kerber, L., & Head, J. W. (2012). A progression of induration in Medusae Fossae Formation transverse aeolian ridges: Evidence for ancient aeolian bedforms and extensive reworking. *Earth Surface Processes and Landforms*, *37*(4), 422–433. https://doi.org/10.1002/esp.2259

Khan, S. Y., Stack, K. M., & Yingst, R. A. (2021). Characterization of Clasts in the Glen Torridon region observed by the MSL curiosity rover. *Paper presented at the 52nd Lunar and Planetary Science Conference, Virtual Meeting*.

Kirk, R. L., & Herkenhoff, K. (2010). Meter-scale topography and slopes of the MSL landing sites from HiRISE stereogrammetry. *4th MSL Landing Site Workshop*.

Kirk, R. L., Howington-Kraus, E., Rosiek, M. R., Anderson, J. A., Archinal, B. A., Becker, K. J., et al. (2008). Ultrahigh resolution topographic mapping of Mars with MRO HiRISE stereo images: Meter-scale slopes of candidate Phoenix landing sites. *Journal of Geophysical Research*, *113*(E3), E00A24. https://doi.org/10.1029/2007JE003000

Kite, E. S., Lewis, K. W., Lamb, M. P., Newman, C. E., & Richardson, M. I. (2013). Growth and form of the mound in Gale Crater, Mars: Slope wind enhanced erosion and transport. *Geology*, *41*(5), 543–546. https://doi.org/10.1130/G33909.1

Kocurek, G., & Ewin, R. C. (2005). Aeolian dune field self-organization—Implications for the formation of simple versus complex dune-field patterns. *Geomorphology*, *72*(1–4), 94–105. https://doi.org/10.1016/j.geomorph.2005.05.005

Kronyak, R. E., Kah, L. C., Miklusicak, N. B., Edgett, K. S., Sun, V. Z., Bryk, A. B., & Williams, R. M. E. (2019). Extensive polygonal fracture network in siccar point group strata: Fracture mechanisms and implications for fluid circulation in Gale Crater, Mars. *Journal of Geophysical Research: Planets*, *124*(10), 2613–2634. https://doi.org/10.1029/2019JE006125

Laity, J. E. (2011). Wind erosion in drylands. In D. S. G. Thomas (Ed.), *Arid zone geomorphology: Process, form and change in drylands* (3rd ed., pp. 539–568). John Wiley.

Landry, W., & Werner, B. T. (1994). Computer simulations of self-organized wind ripple patterns. *Physica D: Nonlinear Phenomena*, *77*(1–3), 238–260. https://doi.org/10.1016/0167-2789(94)90137-6

Lapotre, M. G. A., Ewing, R. C., Lamb, M. P., Fischer, W. W., Grotzinger, J. P., Rubin, D. M., et al. (2016). Large wind ripples on Mars: A record of atmospheric evolution. *Science*, *353*(6294), 55–58. https://doi.org/10.1126/science.aaf3206

Lapotre, M. G. A., & Rampe, E. B. (2018). Curiosity's investigation of the Bagnold Dunes, Gale Crater: Overview of the two-phase scientific campaign and introduction to the special collection. *Geophysical Research Letters*, *45*(19), 10200–102100. https://doi.org/10.1029/2018GL079032

Le Deit, L., Hauber, E., Fueten, F., Pondrelli, M., Pio Rossi, A., & Jaumann, R. (2013). Sequence of infilling events in Gale Crater, Mars: Results from morphology, stratigraphy, and mineralogy. *Journal of Geophysical Research: Planets*, *118*(12), 2439–2473. https://doi.org/10.1002/2012JE004322

Mahaffy, P. R., Webster, C. R., Cabane, M., Conrad, P. G., Coll, P., Atreya, S. K., et al. (2012). The sample analysis at Mars investigation and instrument suite. *Space Science Reviews*, *170*(1–4), 401–478. https://doi.org/10.1007/s11214-012-9879-z

Maki, J. (2013a). *MSL Mars Hazard Avoidance Camera RDR V1.0*. MSL-M-HAZCAM-5-RDR-V1.0. NASA Planetary Data System.

Maki, J. (2013b). *MSL Mars Navigation Camera RDR V1.0*. MSL-M-NAVCAM-5-RDR-V1.0. NASA Planetary Data System.

Maki, J., Thiessen, D., Pourangi, A., Kobzeff, P., Litwin, T., Scherr, L., et al. (2012). The Mars Science Laboratory Engineering Cameras. *Space Science Reviews*, *170*(1–4), 77–93. https://doi.org/10.1007/s11214-012-9882-4

Malin, M. (2013a). *MSL Mars Descent Imager Camera RDR V1.0*. MSL-M-MARDI-4-RDR-IMG-V1.0. NASA Planetary Data System.

Malin, M. (2013b). *MSL Mars Mast Camera RDR V1.0*. MSL-M-MASTCAM-4-RDR-IMG-V1.0. NASA Planetary Data System.

Malin, M. C., Carr, M. H., Danielson, G. E., Davies, M. E., Hartmann, W. K., Ingersoll, A. P., et al. (1998). Early views of the Martian surface from the Mars Orbiter Camera of Mars Global Surveyor. *Science*, *279*(5357), 1681–1685. https://doi.org/10.1126/science.279.5357.1681

Malin, M. C., & Edgett, K. S. (2000). Sedimentary rocks of early Mars. *Science*, *290*(5498), 1927–1937. https://doi.org/10.1126/science.290.5498.1927

Malin, M. C., Ravine, M. A., Caplinger, M. A., Ghaemi, F. T., Schaffner, J. A., Maki, J. N., et al. (2017). The Mars Science Laboratory (MSL) mast cameras and descent imager: Investigation and instrument descriptions. *Earth and Space Science Reviews*, *4*(8), 506–539. https://doi.org/10.1002/2016EA000252

McAdam, A. C., Sutter, B., Archer, P. D., Franz, H. B., Eigenbrode, J. L., Knudson, C. A., et al. (2021). Investigation of the Glen Torridon clay-bearing unit and overlying Greenheugh pediment by the sample analysis at Mars instrument suite. *Presented at the 52nd Lunar and Planetary Science Conference, Virtual Meeting*.

McCauley, J. F. (1973). Mariner 9 evidence for wind erosion in the equatorial and mid-latitude regions of Mars. *Journal of Geophysics Research*, *78*(20), 717–751. https://doi.org/10.1029/jb078i020p04123

McEwen, A. S., Eliason, E. M., Bergstrom, J. W., Bridges, N. T., Hansen, C. J., Delamere, W. A., et al. (2007). Mars Reconnaissance Orbiter's high resolution imaging science experiment (HiRISE). *Journal of Geophysical Research*, *112*(E5), E05S02. https://doi.org/10.1029/2005JE002605

Milliken, R. E., Ewing, R. C., Fischer, W. W., & Hurowitz, J. (2014). Wind-blown sandstones cemented by sulfate and clay minerals in Gale Crater, Mars. *Geophysical Research Letters*, *41*(4), 1149–1154. https://doi.org/10.1002/2013GL059097

Milliken, R. E., Grotzinger, J. P., & Thomson, B. J. (2010). Paleoclimate of Mars as captured by the stratigraphic record in Gale Crater. *Geophysical Research Letters*, *37*(4). https://doi.org/10.1029/2009GL041870

Montgomery, D. R., Bandfield, J. L., & Becker, S. K. (2012). Periodic bedrock ridges on Mars. *Journal of Geophysical Research*, *117*(E3), E03005. https://doi.org/10.1029/2011JE003970

Murchie, S. (2006). MRO CRISM Targeted Reduced Data Record V1.0 [Dataset]. NASA Planetary Data System. https://doi.org/10.17189/1519450

Murchie, S., Arvidson, R., Bedini, P., Beisser, K., Bibring, J.-P., Bishop, J., et al. (2007). Compact Reconnaissance Imaging Spectrometer for Mars (CRISM) on Mars Reconnaissance Orbiter (MRO). *Journal of Geophysical Research*, *112*(E5), E05S03. https://doi.org/10.1029/2006JE002682

Newman, C., Gómez-Elvira, J. G., Marín, M., Navarro, S., Torres, J., Richardson, M. I., et al. (2017). Winds measured by the Rover Environmental Monitoring Station (REMS) during the Mars Science Laboratory (MSL) rover's Bagnold Dunes Campaign and comparison with numerical modeling using MarsWRF. *Icarus*, *291*, 203–231. https://doi.org/10.1016/j.icarus.2016.12.016

Newman, C. E. (2022). Modeling output for orbital and in-situ investigation of periodic bedrock ridges in Glen Torridon, Gale Crater, Mars [Dataset]. Zenodo. https://doi.org/10.5281/zenodo/6514935

Newman, C. E., Kahanpää, H., Richardson, M. I., Martinez, G. M., Vicente-Retortillo, A., & Lemmon, M. (2019). Convective vortex and dust devil predictions for Gale Crater over 3 Mars years and comparison with MSL-REMS observations. *Journal of Geophysical Research: Planets*, *124*(12), 3442–3468. https://doi.org/10.1029/2019JE006082

O'Connell-Cooper, C. D., Thompson, L. M., Gellert, R., Spray, J. G., Boyd, N. I., Berger, J., et al. (2021). APXS Geochemistry of the Fractured Intermediate Unit (fIU) – Its relationship to underlying Glen Torridon units and overlying pediment rocks at the Greenheugh unconformity. *Paper presented at the 52nd Lunar and Planetary Science Conference, Virtual Meeting*.

Pelletier, J. D., Kapp, P. A., Abell, J., Field, J. P., Williams, J. C., & Dorsey, R. J. (2018). Controls on Yardang development and morphology: 1. Field observations and measurements at Ocotillo Wells, California. *Journal of Geophysical Research: Earth Surface*, *123*(4), 694–722. https://doi.org/10.1002/2018JF004629

Perkins, J. P., Finnegan, N. J., & de Silva, S. L. (2015). Amplification of bedrock canyon incision by wind. *Nature Geoscience*, *8*(4), 305–310. https://doi.org/10.1038/NGEO2381

Peters, G. H., Carey, E. M., Anderson, R. C., Abbey, W. J., Kinnett, R., Watkins, J. A., et al. (2018). Uniaxial compressive strengths of rocks drilled at Gale Crater, Mars. *Geophysical Research Letters*, *45*(1), 108–116. https://doi.org/10.1002/2017GL075965

Rampe, E. B., Bristow, T. F., Morris, R. V., Morrison, S. M., Achilles, C. N., Ming, D. W., et al. (2020). Mineralogy of Vera Rubin ridge from the Mars Science Laboratory CheMin instrument. *Journal of Geophysical Research: Planets*, *125*(9), e2019JE006306. https://doi.org/10.1029/2019JE006306

Rapin, W., Dromart, G., Rubin, D., Le Deit, L., Mangold, N., Edgar, L. A., et al. (2021). Alternating wet and dry depositional environments recorded in the stratigraphy of Mount Sharp at Gale Crater, Mars. *Geology*, *49*(7), 842–846. https://doi.org/10.1130/G48519.1

Rice, M. S., Gupta, S., Treiman, A. H., Stack, K. M., Calef, F., Edgar, L. A., et al. (2017). Geologic overview of the Mars Science Laboratory rover mission at the Kimberley, Gale Crater, Mars. *Journal of Geophysical Research: Planets*, *122*(1), 2–20. https://doi.org/10.1002/2016JE00500

Richardson, M. I., Toigo, A. D., & Newman, C. E. (2007). PlanetWRF: A general purpose, local to global numerical model for planetary atmospheric and climate dynamics. *Journal of Geophysical Research*, *112*(E9), E09001. https://doi.org/10.1029/2006JE002825

Rivera-Hernández, F., Sumner, D. Y., Mangold, N., Stack, K. M., Forni, O., Newsom, H., et al. (2019). Using ChemCam LIBS data to constrain grain size in rocks on Mars: Proof of concept and application to rocks at Yellowknife Bay and Pahrump Hills, Gale Crater. *Icarus*, *321*, 82–98. https://doi.org/10.1016/j.icarus.2018.10.023

Schieber, J., Minitti, M., Sullivan, R., Edgett, K. S., Malin, M. C., Parker, T., & Calef, F. (2020). Engraved on the rocks—Aeolian abrasion of Martian mudstone exposures and their relationship to modern wind patterns in Gale Crater, Mars. *The Depositional Record*, *6*(3), 625–647. https://doi.org/10.1002/dep2.110

Silvestro, S., Pacifici, A., Salese, F., Vaz, D. A., Neeseman, A., Tirsch, D., et al. (2021). Periodic bedrock ridges at the ExoMars 2022 landing site: Evidence for a changing wind regime. *Geophysical Research Letters*, *48*(4). https://doi.org/10.1029/2020GL091651

Sneed, J., Stack, K., Day, M. D., & Fraeman, A. (2020). Large-scale HiRISE survey demonstrates a genetic relationship between Martian periodic bedrock ridges and transverse aeolian ridges. *Presented at the American Geophysical Union, Fall Meeting 2020, Virtual Meeting*.

Stack, K. M. (2021). Shapefiles for Glen Torridon bedrock ridges, ripples, transverse aeolian ridges, wavelength, and topographic profiles (version 1) [Dataset]. Zenodo. https://doi.org/10.5281/zenodo.6324330

Stack, K. M., Edwards, C. S., Grotzinger, J. P., Gupta, S., Sumner, D. Y., Calef, F. J., III, et al. (2016). Comparing orbiter and rover image-based mapping of an ancient sedimentary environment, Aeolis Palus, Gale Crater, Mars. *Icarus*, *280*, 3–21. https://doi.org/10.1016/j.icarus.2016.02.024

Stack, K. M., Grotzinger, J. P., Lamb, M. P., Gupta, S., Rubin, D. M., Kah, L. C., et al. (2019). Evidence for plunging river plume deposits in the Pahrump Hills member of the Murray formation, Gale Crater, Mars. *Sedimentology*, *66*(5), 1768–1802. https://doi.org/10.1111/sed.12558

Stein, N. T., Quinn, D. P., Grotzinger, J. P., Fedo, C., Ehlmann, B. L., Stack, K. M., et al. (2020). Regional structural orientation of the Mount Sharp group revealed by in situ dip measurements and stratigraphic correlations on the Vera Rubin ridge. *Journal of Geophysical Research: Planets*, *125*(5). https://doi.org/10.1029/2019JE006298

Sullivan, R., Arvidson, R., Bell, J. F., III, Gellert, R., Golombek, M., Greeley, R., et al. (2008). Wind-driven particle mobility on Mars: Insights from Mars exploration observations at "El Dorado" and surroundings at Gusev Crater. *Journal of Geophysical Research*, *113*(E6), E06S07. https://doi.org/10.1029/2008JE003101

Sullivan, R., Baker, M., Edgar, L., Herkenhoff, H., & Weitz, C. (2020). The aeolian environment of Glen Torridon, Mars, observed by the MSL rover. *Paper presented at the 51st Lunar and Planetary Science Conference*.

Sullivan, R., Banfield, D., Bell, J. F., III, Calvin, W., Fike, D., Golombek, M., et al. (2005). Aeolian processes at the Mars exploration rover Meridiani Planum landing site. *Nature*, *438*(7047), 58–61. https://doi.org/10.1038/nature03641

Thomas, P., Veverka, J., Lee, S., & Bloom, A. (1981). Classification of wind streaks on Mars. *Icarus*, *45*(1), 124–153. https://doi.org/10.1016/0019-1035(81)90010-5

Thomson, B. J., Bridges, N. T., Milliken, R. E., Baldridge, A., Hook, S. J., Crowley, J. K., et al. (2011). Constraints on the origin and evolution of the layered mound in Gale Crater, Mars using Mars Reconnaissance Orbiter data. *Icarus*, *214*(2), 413–432. https://doi.org/10.1016/j.icarus.2011.05.002

Thorpe, M. T., Bristow, T. F., Rampe, E. B., Grotzinger, J. P., Fox, V. K., Bennett, K. A., et al. (2021). The mineralogy and sedimentary history of the Glen Torridon region, Gale Crater, Mars. *Paper presented at the 52nd Lunar and Planetary Science Conference, Virtual Meeting*.

Tirsch, D., Jaumann, R., Pacifici, A., & Poulet, F. (2011). Dark aeolian sediments in Martian craters: Composition and sources. *Journal of Geophysical Research: Planets*, *116*(E3), E03002. https://doi.org/10.1029/2009JE003562

Vasavada, A. R., Grotzinger, J. P., Arvidson, R. E., Calef, F. J., Crisp, J. A., Gupta, S., et al. (2014). Overview of the Mars Science Laboratory mission: Bradbury landing to Yellowknife Bay and beyond. *Journal of Geophysical Research: Planets*, *119*(6), 1134–1161. https://doi.org/10.1002/2014JE004622

Vasavada, A. R., Piquex, S., Lewis, K. W., Lemmon, M. T., & Smith, M. D. (2017). Thermophysical properties along Curiosity's traverse in Gale Crater, Mars, derived from the REMS ground temperature sensor. *Icarus*, *284*, 372–386. https://doi.org/10.1016/j.icarus.2016.11.035

Veverka, J., Gierasch, P., & Thomas, P. (1981). Wind streaks on Mars: Meterological control of occurrence and mode of formation. *Icarus*, *45*(1), 154–166. https://doi.org/10.1016/0019-1035(81)90011-7

Wang, J., Xiao, L., Reiss, D., Hiesinger, H., Huang, J., Xu, Y., et al. (2018). Geological features and evolution of Yardangs in the Qaidam Basin, Tibetan Plateau (NW China): A terrestrial analogue for Mars. *Journal of Geophysical Research: Planets*, *123*(9), 2336–2364. https://doi.org/10.1029/2018JE005719

Ward, A. W. (1979). Yardangs on Mars: Evidence of recent wind erosion. *Journal of Geophysical Research*, *84*(B14), 8147. https://doi.org/10.1029/JB084iB14p08147

Ward, A. W., Doyle, K. B., Helm, P. J., Weisman, M. K., & Witbeck, N. E. (1985). Global map of eolian features on Mars. *Journal of Geophysical Research*, *90*(B2), 2038. https://doi.org/10.1029/JB090iB02p02038

Weitz, C. M., Sullivan, R. J., Baker, M., & Grant, J. M. (2021). Aeolian bedform grain properties at Gale Crater from Vera Rubin ridge to the sands of Forvie. *Paper presented at the 52nd Lunar and Planetary Science Conference*.

Weitz, C. M., Sullivan, R. J., Lapotre, M. G. A., Rowland, S. K., Grant, J. A., Baker, M., & Yingst, R. A. (2018). Sand grain sizes and shapes in eolian bedforms at Gale Crater, Mars. *Geophysical Research Letters*, *45*(18), 9471–9479. https://doi.org/10.1029/2018GL078972

Williams, R. M. E., & Weitz, C. (2014). Reconstructing the aqueous history within the southwestern Melas basin, Mars: Clues from stratigraphic and morphometric analyses of fans. *Icarus*, *242*, 19–37. https://doi.org/10.1016/j.icarus.2014.06.030

Zimbelman, J. R. (2010). Transverse aeolian ridges on Mars: First results from HiRISE images. *Geomorphology*, *121*(1–2), 22–29. https://doi.org/10.1016/j.geomorph.2009.05.012

Zimbelman, J. R., & Foroutan, M. (2020). Dingo Gap: Curiosity went up a small transverse Aeolian Ridge and came down a megaripple. *Journal of Geophysical Research: Planets*, *125*(12). https://doi.org/10.1029/2020JE006489

Zimbelman, J. R., & Griffin, L. J. (2010). HiRISE images of Yardangs and sinuous ridges in the lower member of the Medusae Fossae Formation, Mars. *Icarus*, *205*(1), 198–201. https://doi.org/10.1016/j.icarus.2009.04.003

Zurek, R. W., & Smrekar, S. E. (2007). An overview of the Mars Reconnaissance Orbiter (MRO) science mission. *Journal of Geophysical Research*, *112*(E5), E05S01. https://doi.org/10.1029/2006JE002701